HHS Public Access

Author manuscript

Neurochem Int. Author manuscript; available in PMC 2021 February 01.

Published in final edited form as:

Neurochem Int. 2020 February ; 133: 104628. doi:10.1016/j.neuint.2019.104628.

Potassium and glutamate transport is impaired in scar-forming tumor-associated astrocytes

Susan C. Campbell[a,2], **Carmen Muñoz-Ballester**[b,2], **Lata Chaunsali**[b,c], **William A. Mills III**[d,e], **Jennifer H. Yang**[f], **Harald Sontheimer**[b,d,**,1], **Stefanie Robel**[b,d,*,1]

[a]Animal and Poultry Science, Virginia Tech, Blacksburg, VA, 24061, USA

[b]Fralin Biomedical Research Institute at Virginia Tech Carilion, Roanoke VA, 24016, USA

[c]Molecular and Cellular Biology Graduate Program at Virginia Tech, Blacksburg, VA, 24061, USA

[d]Virginia Tech School of Neuroscience, Blacksburg, VA, 24060, USA

[e]Graduate Program in Translational Biology, Medicine, and Health, Virginia Tech, Roanoke, 24016, USA

[f]University of Alabama at Birmingham, Birmingham, AL, 35294, USA

Abstract

Unprovoked recurrent seizures are a serious comorbidity affecting most patients who suffer from glioma, a primary brain tumor composed of malignant glial cells. Cellular mechanisms contributing to the development of recurrent spontaneous seizures include the release of the excitatory neurotransmitter glutamate from glioma into extracellular space. Under physiological conditions, astrocytes express two high affinity glutamate transporters, Glt-1 and Glast, which are responsible for the removal of excess extracellular glutamate. In the context of neurological disease or brain injury, astrocytes become reactive which can negatively affect neuronal function, causing hyperexcitability and/or death. Using electrophysiology, immunohistochemistry, fluorescent in situ hybridization, and Western blot analysis in different orthotopic xenograft and allograft models of human and mouse gliomas, we find that peritumoral astrocytes exhibit astrocyte scar formation characterized by proliferation, cellular hypertrophy, process elongation, and increased GFAP and pSTAT3. Overall, peritumoral reactive astrocytes show a significant reduction in glutamate and potassium uptake, as well as decreased glutamine synthetase activity.

[*]Corresponding author. 2 Riverside Circle, Roanoke, VA, 24016, USA. sontheim@vt.edu (H. Sontheimer). [**]Corresponding author. 2 Riverside Circle, Roanoke, VA, 24016, USA. srobel@vt.edu (S. Robel).

[1]Shared last authorship.

[2]Shared first authors, authors contributed equally to the manuscript.

CRediT authorship contribution statement

Susan C. Campbell: Conceptualization, Methodology, Investigation, Formal analysis, Writing - original draft. **Carmen Muñoz-Ballester:** Methodology, Validation, Formal analysis, Investigation, Writing - review & editing, Visualization, Project administration. **Lata Chaunsali:** Methodology, Validation, Formal analysis, Investigation, Writing - review & editing, Visualization. **William A. Mills:** Formal analysis. **Jennifer H. Yang:** Formal analysis, Investigation. **Harald Sontheimer:** Conceptualization, Resources, Supervision, Funding acquisition. **Stefanie Robel:** Conceptualization, Methodology, Validation, Formal analysis, Investigation, Resources, Writing - original draft, Writing - review & editing, Visualization, Supervision, Project administration, Funding acquisition.

Appendix A. Supplementary data

Supplementary data to this article can be found online at https://doi.org/10.1016/j.neuint.2019.104628.

A subset of peritumoral astrocytes displayed a depolarized resting membrane potential, further contributing to reduced potassium and glutamate homeostasis. These changes may contribute to the propagation of peritumoral neuronal hyperexcitability and excitotoxic death.

Keywords

Acquired epilepsy; Tumor-associated epilepsy; Astrogliosis; Reactive astrocytes; Seizures; Glial scar

1. Introduction

Unprovoked seizures are experienced by 60–80% of patients with primary brain tumors (Kurzwelly et al., 2010; Lynam et al., 2007; Reif et al., 2010; Ross et al., 2018). In fact, a seizure will often be the first symptom that leads to the diagnosis of a brain tumor. Primary brain tumors occur with an incidence of 18 per 100,000 every year in the United States, and approximately two thirds of all primary brain tumors are gliomas, malignant tumors comprised of glial cells (Porter et al., 2010). Tumor-associated epilepsy is a debilitating comorbidity of glioma that severely impacts the already sick patient. Traditional anti-epileptic drugs are often ineffective and seizures might only be controllable by surgical resection of the tumor. However, the majority of patients will again suffer from seizures after tumor recurrence. The anti-epileptic drugs used to treat tumor-associated seizures have side effects that further decrease the patient's quality of life.

Cellular mechanisms contributing to the development of recurrent spontaneous seizures include the release of the excitatory neurotransmitter glutamate from glioma into the extracellular space via the system x(c) (−) cystine-glutamate transporter (encoded by Slc7a11) (Buckingham et al., 2011). High expression of this co-transporter is associated with seizures in glioma patients and predicts their poor survival (Robert et al. 2015). In the healthy brain, astrocytes are responsible for the removal of excess extracellular glutamate via their high affinity electrogenic transporters Glt-1 (EAAT2) and Glast (EAAT1), which are driven by the ion gradients of sodium and potassium. Glt-1 has a binding affinity for glutamate of KD = 20 μM and transports about 30 glutamate molecules per second. To maintain extracellular glutamate concentrations as low as 25 nM, Glt-1 is one of the most abundantly expressed proteins in the brain by itself, accounting for about 1% of the total protein (Zhou and Danbolt, 2013). Thus astrocytes are well equipped to buffer increased extracellular glutamate even in the presence of glioma cells as recently shown in culture. However, when the ratio between cultured astrocytes and glioma cells becomes too small, extracellular glutamate concentrations increase (Yao et al., 2014). Additionally, astrocytes can become impaired in their ability to provide brain homeostasis in the context of brain injury or neurological diseases (Bedner et al., 2015; Olsen et al., 2015; Seifert et al., 2006).

A property of all astrocytes is their ability to sense and react to brain insult with the process of astrogliosis. In the context of severe acute traumatic brain or spinal cord injury, reactive astrocytes form a protective scar that seals injured central nervous system (CNS) areas off. Removal of these scar-forming astrocytes results in worsened outcomes after CNS trauma (Anderson et al., 2016; Bush et al., 1999; Faulkner et al., 2004). In other neurological

diseases, astrogliosis does not always result in scar formation but even milder types of reactive astrocytes appear to come at the price of faulty support for neurons. The result can be neuronal dysfunction, hyperexcitability and/or death (Liddelow et al., 2017; Robel et al., 2015; Shandra et al., 2019; Tong et al., 2014).

Accumulating evidence from human subjects and animal models demonstrates that reactive astrocyte dysfunction contributes to seizure activity and epileptogenesis (Wetherington et al., 2008). The most prominent example is mesio-temporal lobe epilepsy, where decades of research implicate astrocytes in the genesis of seizures (Robel, 2016; Trachtenberg and Pollen, 1970) and removal of the glial scar is essential for seizure control in temporal lobe epilepsy patients that are refractory to anti-epileptic drugs (AED's). Numerous studies have provided compelling evidence that reactive astrocytes are dysfunctional in their ability to maintain a local ion and transmitter milieu suitable to sustain normal neuronal activity (Robel and Sontheimer, 2015; Shandra et al., 2019). Direct evidence that astrogliosis is causal was provided in a study inducing astrogliosis virally, which induces epileptiform activity in hippocampal slices (Ortinski et al., 2010). In a genetic model of astrogliosis, elimination of β1-integrins in the astrocytic lineage causes widespread chronic astrogliosis and subsequent development of spontaneous recurrent seizures (Robel et al., 2015). Similarly, Alexander disease, which is caused by point mutations in the astrocytic intermediate filament glial fibrillary acidic protein (GFAP), results in severe reactive gliosis, seizures, and developmental delay (Brenner et al., 2001). Yet, despite the reliability of the astrogliosis response, the process is highly heterogeneous with a plethora of graded alterations to gene & protein expression, the secretome, morphology and astrocyte function (Sofroniew, 2014) that depend on the disease context and modifies astrocyte-neuronal interactions in highly specific ways. Here, we tested the hypothesis that glioma-induced astrogliosis renders peritumoral astrocytes dysfunctional, perpetuating the imbalance between excitation and inhibition in tumor-associated epilepsy.

2. Materials and methods

2.1. Animals

2.1.1. General—Adult 8–12 week old mice of both sexes and homozygous for the immune deficiency mutation Prkdc^{scid} (*C.B.17 scid),* commonly referred to as scid mice, were used for tumor implantations. Immunodeficiency is required to allow growth of tissues derived from a different species, which would otherwise be suppressed by the host's immune system. Colonies were maintained in a standard pathogen free barrier animal facility in groups of 5 animals at maximum on a 12 h light//12 h dark cycle. Mice had access to food and water ad libitum. Mice were bred in-house; some scid mice were purchased from Charles River. All animal procedures were approved and performed according to the guidelines of the Institutional Animal Care and Use Committee (IACUC) of the University of Alabama at Birmingham and Virginia Tech and were conducted in compliance with the National Institutes of Health's “Guide for the Care and Use of Laboratory Animals.”

2.1.2. Immunodeficient Aldh1l1-eGFP mice—Swiss Webster-Aldh1l1-eGFP bacterial artificial chromosome (BAC) transgenic mice (generated by the GENSAT project)

were crossed to C.B.17 scid mice and genotyped for the Prkdc^{scid} point mutation as previously described (Maruyama et al., 2002). Mice homozygous for the Prkdc^{scid} mutation and positive for GFP (Aldh1l1-eGFP-scid) were maintained as a colony for more than 10 generations and offspring of either sex was used for experiments.

2.2. Glioma cells

2.2.1. Patient-derived xenograft tumor lines—GBM22 patient xenograft cells were derived from primary brain tumor tissue (generous gift by Dr. Yancey Gillespie, University of Alabama at Birmingham, Birmingham, AL, USA) and maintained by serial passage in the flank of athymic nude mice, as previously described (Giannini et al., 2005). Tumors were harvested, mechanically dissociated, and maintained in culture as spheres in Neurobasal-A medium (Invitrogen) supplemented with 10 mg ml-1 of EGF and FGF (Invitrogen), 250 μM ml-1 amphotericin, 50 mg ml-1 gentamycin (Fisher), 260 mM L-glutamine (Invitrogen), and 10 ml B-27 supplement without Vitamin A (Invitrogen). Xenograft cells were maintained as spheres in vitro for 5–7 days before intracranial injections in scid or Aldh1l1-eGFP-scid mice. All electrophysiology and western blot experiments used the human xenocraft line GBM22 (see above).

2.2.2. D54 glioma cell line—For histological analysis of the relationship between astrocytes and glioma cells, mice were stereotactically implanted with either human glioma cells derived from D54-MG (*D54*) glioma cells (WHO IV, glioblastoma multiforme; Dr. D. Bigner, Duke University, Durham, NC) that were stably transfected with *pEGFP-N1* (Clonetech). A red fluorescing D54 tumor cell line was generated as described before (Watkins et al., 2014).

2.3. Inoculation of (Aldh1l1-eGFP)-scid mice with glioma

Human or mouse glioma cells were implanted into 6–12 week old immunodeficient *C.B.-17 scid* or *Aldh1l1-eGFP-scid* mice of either sex. Animals were anesthetized by 2–5% isoflurane and a midline scalp incision was created. A 0.5 mm burr hole was made at 1.0–2.0 mm and 0.5–1.0 mm posterior from bregma. *D54-EGFP* human glioma cells (1.25–5.0 × 10^5) or GBM22 patient-derived xenograft tumors (1.0–1.5 × 10^5) were injected into one hemisphere at 1–2 mm depth (z axis at an angle of 35°). Following surgery, the animals were placed in a heating pad until recovery to minimize post-procedure suffering. Intracranial tumors grew for 2–4 weeks. Body weight was monitored periodically and mice with loss of body weight indicating tumor growth were chosen for experiments. If the glioma was not distinguishable after 2–4 weeks, the animal was excluded.

2.4. Histological procedures

2.4.1. Perfusion—Mice were deeply anesthetized with ketamine and xylazine prior to transcardial perfusion with phosphate-buffered saline (PBS) followed by 4% paraformaldehyde (PFA). Brain tissue was collected and post-fixed in 4% PFA overnight. Coronal slices were cut at 40–50 μm thickness using a vibratome (Campden 5100mz).

2.4.2. Immunohistochemistry—Immunohistochemistry was performed using primary antibodies as specified in Table 1 in PBS with 0.5% Triton X and 10% goat serum at 4

°C overnight. Slices were washed in PBS and incubated in secondary antibodies (Table 1) in 1x PBS with 0.5% Triton X and 10% goat serum for 1–2 h at room temperature. 4,6-Diamidino-2-phenylindole (DAPI) was included in the secondary antibody solution. Slices were washed in PBS and mounted on glass microscope slides using Aqua Poly/Mount (Polysciences, Inc., Cat. #18606). For pSTAT3 stainings, samples were pretreated by heating in EDTA-HCl pH9.0 buffer at 95 °C for 10 min prior to the antibody incubation. For rat anti-C3 stainings, samples were pretreated with sodium citrate 10 mM, pH6, at 80 °C for 30 min and the primaries and secondaries were diluted in 0.3% Triton X and 10% goat serum.

Nissl staining- After secondary antibody incubation slices were washed with PBS 2–3 times for 5 min each, they were permeabilized with 0.5% Triton X in PBS for 10 min followed by a 10 min wash in PBS. Slices were incubated with NeuroTrace at 1:100 dilution in PBS for 20 min. Slices were again washed with 0.5% Triton X for 10 min followed by 10 min wash in PBS.

Images of sham, naive and tumor-bearing mice were acquired using an Olympus or a Nikon A1R confocal microscope with Nikon 4x, 10x or 20x air objectives or Nikon Apo 40×/1.30 and 60x/1.40 oil immersion objectives.

2.4.3. Hematoxylin & Eosin staining—All the products described in this protocol were available in the Hematoxylin & Eosin Stain Kit (Vector Laboratories). Stainings were performed as indicated by the manufacturer. Floating 40–50 μm brain sections were mounted on Inkjet Plus Microscope Slides (Fisher Scientific) and dried until the tissue was completely attached to the surface (1 h approximately). Slides were then rinsed in water for 5 s. Hematoxylin was applied to completely cover the tissue sections and incubated for 5 min. Slides were rinsed in two changes of distilled water (15 s each) to remove excess stain. Bluing reagent was applied to completely cover the tissue and incubated for 15 s. Slides were rinsed in 2 changes of distilled water (15 s each). Slides were dipped in 100% ethanol (10 s). Eosin Y solution was applied completely covering the tissue, incubated for 3 min, and washed in 100% ethanol for 10 s. Finally, the slide was dehydrated in 3 changes of 100% ethanol and mounted in VectaMount Mounting Medium (Vector laboratories). Images were acquired at an Olympus vs-120 microscope using a 20x objective and processed in ImageJ.

2.5. Western blots

GBM22 tumor-bearing mice were sacrificed by cervical dislocation 2–4 weeks after inoculation. Brains were sliced using a vibratome and peritumoral or contralateral tissue was collected using a tissue puncher with 0.5 mm diameter. Tissue punches were collected in lysis buffer and samples were rapidly frozen on dry ice and stored at −80 °C until further processing.

Tissues were mechanically homogenized in radioimmunoprecipitation assay (RIPA) buffer with 1:100 protease and phosphatase inhibitors (Sigma-Aldrich, Cat. P8340, P0044) followed by sonication (3 × 10s pulse/Rest 5s, 30% amplitude) on ice. Remaining tissue fragments were spun down and protein supernatants were stored at −80 °C. Protein concentrations were determined for each sample using a Bicinchoninic acid (BCA) assay.

5–10 μg protein was mixed with sample buffer (4x Laemmli sample buffer with beta-mercaptoethanol) and 1:10 dithiothreitol (DTT), denatured at 95 °C for 10 min, and loaded into 4–20% BioRad Criterion TGX precast gels. Gels were run at 80 V until the dye line narrowed and then at 200 V for ~30–45 min. The Trans-blot Turbo Transfer system was used for semi-dry transfer at 2.5A and 25 V for 10 min. Membranes were blocked in 5% nonfat milk (NFM) in tris-buffered saline-tween 20 (TBST) for 30 min. Membranes were incubated in primary antibody solution (Table 2) in 5% NFM/TBST overnight at 4 °C. Membranes were washed and incubated in secondary antibody solution in 5% NFM/TBST for 1 h at room temperature. Membranes were developed with luminol/peroxide developer solution (Table 2) and immediately imaged with the Azure c500 imaging system.

2.6. RNAScope

Brain tissue was collected as previously described in section 2.4 and post-fixed in 4% PFA overnight. Coronal slices were cut at 40–50 μm thickness using a vibratome (Campden 5100mz). Floating sections were mounted on glass slides followed by in situ hybridization according to the manufacturer's instructions (Advanced Cell Diagnostics, Hayward, CA, USA). We used the RNAscope® Probe Mm-Kcnj10-C3 (Advance Cell Diagnostics, Hayward, CA, USA, Cat # 458831-C3) to detect Kir4.1 transcripts, using the RNAscope Multiplex Fluorescent Reagent Kit v2 assay amplification kit (Advance Cell Diagnostics, Hayward, CA, USA, cat # 323100). Images were acquired using a 40x objective with a Nikon AIR confocal microscope and analyzed using the “analyze particles” tool in ImageJ (objects selected 0–50 pixels; circularity 0–1).

2.7. Electrophysiology

2.7.1. Whole-cell patch clamp recordings—Animals were decapitated, the brains removed and immersed in ice-cold cutting solution (in mM): 135 N-methyl-D-gluconate (NMDG), 1.5 KCl, 1.5 KH2PO4, 23 choline bicarbonate, 25 D-glucose, 0.5 CaCl2, 3.5 MgSO4. Coronal slices (300 μm) recovered in normal recording solution (in mM): 125 NaCl, 3 KCl, 1.25 NaH2PO4, 25 NaHCO3, 2 CaCl2, 1.3 MgSO4, 25 D-glucose at 37 °C for 1 h before recording. Whole-cell patch clamp recordings were obtained using an intracellular solution consisting of (in mM): 134 K-gluconate, 1 KCl, 10 HEPES, 2 Mg-ATP, 0.2 Na-GTP, and 0.5 EGTA, pH 7.4, 285–290 mOsm. Tight seals were established using patch electrodes (KG-33 glass, Garner Glass) with a 5–8 MΩ open-pipette resistance at −80 mV for astrocytes as previously described (Olsen et al., 2006). Astrocytes were visualized using a Zeiss Axioscope microscope, a 40× water immersion objective, and epifluorescent illumination (GFP-positive astrocytes in Aldh1l1-eGFP mice). Drugs were added to the recording solution (50 μM D-AP5, 20 μM CNQX, 500 nM tetrodotoxin (TTX), 0.1 mM CdCl2 (Sigma), 0.1 μM BaCl2 (Sigma), 20 μM bicuculline methiodide, 0.3 mM DL-threo-β-Benzyloxyaspartic acid (TBOA), 0.4 mM dihydrokainic acid (DHK). Unless stated otherwise, all drugs were purchased from Tocris. Data were acquired using Clampex 10 software and a 19 Digidata 1440A interface (Molecular Devices), filtered at 5 kHz, digitized at 10–20 kHz, and analyzed using Clampfit 10.0 software (Molecular Devices). Resting membrane potentials (RMPs) (in I = 0 mode), whole-cell capacitance, and series resistances were measured directly from the amplifier, after whole cell access was obtained.

Series resistance compensation was adjusted to 85% to reduce voltage errors. Slices were continuously perfused with artificial cerebral spinal (ACSF) fluid at 34 °C.

Pressure application of potassium or glutamate was performed using the Pico-Liter Injector PLI-10 (Warner Instruments) at an injection pressure of 1–2 PSI for 50 ms (K+ uptake) or 500 ms (Glutamate uptake). Uptake was recorded three times for each cell and condition. Traces were averaged before analysis.). For recordings of evoked inhibitory postsynaptic currents (eIPSCs), cells were held at −40 mV in the presence of APV (50 μM) and CNQX (20 μM). In experiments involving inhibition of glutamine synthetase, slices were preincubated in ACSF containing methionine sulfoximine (MSO, 1.5 mM) for at least 1.5 h. For experiments with exogenous glutamine application, glutamine (10 mM) was applied to slices at least 15 min before recordings. All electrophysiology experiments were performed in acute brain slices of GBM22-bearing animals or controls. Of 36 animals in the “glioma group”, one was excluded in this study due to the absence of a tumor.

2.8. Data analysis

2.8.1. Quantification of phospho-STAT3-positive astrocytes—To quantify pSTAT3+ astrocytes, confocal images were taken in 3–5 different slices of each animal (n = 3 animals). Per slice, 3–5 pictures were taken in 1) a region of interest (ROI) at < 300 μm from the tumor, 2) a ROI at > 300 μm from the tumor and 3) ROIs in equivalent areas of the contralateral hemisphere. Confocal images had a z-step size of 0.7 μm and the Aldh1l1-eGFP + cells (astrocytes) and pSTAT3+/Aldh1l1-eGFP + cells (pSTAT3+ astrocytes) in the case of Aldh1l1-eGFP GBM22 animals were quantified manually step-by-step using the cell counter tool in ImageJ. In the case of Scid-D54-GFP animals, astrocytes were identified as S100β+ cells and were manually quantified using the cell counter tool in ImageJ step-by-step in z-stack images. S100β+/pSTAT3+ cells were quantified in a similar way.

2.8.2. Quantification of Kir4.1 gray value intensity—To quantify Kir4.1 expression, we collapsed confocal z-stack images in a z-projection using the Nikon analysis program NIS-Elements AR Analysis 4.40.00. Using the Graticule function (a grid where the center is fixed and establishes 100 μm distant concentric circles from that center), we fixed the center of the grid at the edge of the tumor in the image and determined areas of 100, 200, 300 and 400 μm from the edge of the tumor. Using ImageJ, we quantified the mean gray value of the areas 100, 200, 300 and 400 μm from the edge of the tumor in the Kir4.1 channel.

2.8.3. Quantification of astrocyte proliferation—Astrocyte proliferation was assessed using immunohistochemistry against the cell cycle protein Ki67. To quantify the number of Ki67 + astrocytes, confocal images were taken within the cortical gray matter in 3–5 different slices per animal, in 1) regions of interest (ROIs) surrounding the tumor (n = 5 animals), 2) ROIs in equivalent cortical areas of the contralateral hemisphere (n = 5 animals) or 3) Sham animals (n = 3). Confocal images had a z-step size of 1 μm, stacks spanned the entire slice, and were quantified step-by-step using the cell counter tool in ImageJ. Cells that co-labeled for GFP/DAPI and Ki67 were considered proliferating astrocytes.

2.8.4. Quantification of western blot data—Blots were quantified with Azurespot analysis software. Images were converted to grayscale for band quantification. Lane detection software prevented lane overlap and accounted for the curvature of some lanes. Rolling ball background subtraction was used for each blot image. Automatic band detection was first used to detect band peak gray values, followed by manual adjustment to restrict the area of band measurement to the band edges. Gray values of each band were measured in the above-defined frames. Band gray values were divided by band gray values of a GAPDH or tubulin loading control to determine relative protein levels for each sample. Values for peritumoral and contralateral samples of the same animal were paired for statistical analysis.

2.8.5. Quantification of electrophysiology data—In potassium uptake experiments, Kir4.1-sensitive currents were determined by subtracting the currents induced by pressure application of potassium before and after bath application of barium. Glutamate transporter currents were measured before and after application of glutamate transporter inhibitors TBOA and DHK. eIPSC amplitudes were calculated before and after burst stimulation protocol. For controls, both acute slices from naive or sham-injected animals were used. No significant differences were noted with respect to resting membrane potential, cell capacitance, or potassium uptake currents. Hence, both control groups were pooled. Astrocytes with input resistances of higher than 50 MΩ were excluded from the analysis (typical input resistances ranged from 5 to 25 MΩ), as were astrocytes that died within 5 min after the cell was opened or before the experiment was completed, e.g. astrocytes were excluded for analysis of glutamate uptake if the cell died or increased in input resistance by more than 15 MΩ before the TBOA/DHK inhibitor was washed in and the glutamate uptake current was recorded in the presence of the inhibor.

2.8.6. Experimental design and statistics—This study was not pre-registered. Animals were assigned to a cage randomly when weaned. Before the experiment, cages were randomly distributed into experimental groups (“Sham” and “glioma”). For each experiment, groups included “Control” and “glioma” animals, except for pSTAT3, Sox9, C3, and cleaved-caspase 3 stainings and western blot analysis, in which the glioma-bearing hemisphere was compared to the contralateral hemisphere. A total of 44 animals (8 shams and 36 glioma animals) were used. Control animals were either injected with sterile PBS free of glioma cells (sham) or left naïve since intracranial injections of any kind will induce astrogliosis and scar formation along the needle track. In every injection session, glioma animals were injected before sham animals. Tumors were allowed to grow for 2–4 weeks. Animals were euthanized for experiments once they started losing weight, which indicated tumor growth (Fig. 1). Sample sizes were chosen based on previous studies (Kimbrough et al., 2015; Watkins et al., 2014).

Data were tested for normal distribution using the Kolmogorov–Smirnov (KS) normality test. Statistical tests were chosen as appropriate and are specified in the results or figure legends. Unless stated otherwise, all values are reported as mean with SEM.

Statistics were computed and graphed with GraphPad Prism 7 (GraphPad Software). The significance level was set to $p \leq 0.05$. Scatter plots display individual values and bar graphs

display the mean with SEM. Statistical significance is indicated with *$p \leq 0.05$, **$p \leq 0.01$, ***$p \leq 0.001$, ****$p \leq 0.0001$.

3. Results

3.1. Peritumoral astrocytes contribute to scar formation

To determine if glioma growth induced an astrocyte response, we inoculated the cortical gray matter of immune-compromised scid or Aldh1l1-eGFP-scid mice with two different glioma lines. Human D54 glioma cells have been classically used in many studies and GBM22 is a patient-derived glioma xenoline that has been propagated in the flank of nude mice rather than in culture to better maintain the original biological properties of the tumor (Giannini et al., 2005). The implanted glioma cells grew into a mass within the cortical gray matter after 2–4 weeks dependent on the cell line or success of inoculation.

The astrocytic glial fibrillary acidic protein (GFAP) is typically increased in response to neurological disease and brain injury, yet expressed at low levels in the uninjured mouse cortical gray matter (Fig. 2a, g, h). Astrocytes surrounding gliomas (peritumoral astrocytes) responded by strongly upregulating GFAP independent of the glioma type (Fig. 2b-i) (relative expression levels of GBM22 peritumoral tissue normalized to GAPDH: contralateral 1.3 ± 0.4 n = 6; peritumoral 6.3 ± 1.1 n = 6, two-tailed paired *t*-test p = 0.0054).

Astrocytes directly adjacent to the tumor mass were elongated in morphology similar to scar-forming astrocytes surrounding focal brain injury (Robel et al., 2015). Astrocytes in areas beyond this astroglial scar were not elongated but hypertrophic with swollen GFAP-positive processes (Fig. 2i). In the contralateral hemisphere, astrocytes only upregulated GFAP when the tumor had grown so large that a midline shift occurred (Fig. 2g, second sample set).

Hematoxylin and Eosin stainings of GBM22 and D54 tumor-bearing tissue outline the tumors based on their acidic nature, and hence, more deeply blue color. The peritumoral region also appears more acidic when compared to control tissue (Fig. 2j).

3.2. Peritumoral astrocytes have a variable molecular signature

Phosphorylation of the cytokine and growth factor signal transducer and activator of transcription 3 (pSTAT3), which regulates genes involved in astrogliosis including GFAP, is essential for the formation of astroglial scars borders in the spinal cord (Herrmann et al., 2008; Wanner et al., 2013). To determine if pSTAT3 was increased in peritumoral astrocytes, we performed immunohistochemistry and determined the percentage of Aldh1l1-eGFP+ (for GBM22) or S100β+ (for D54) astrocytes that co-labeled for pSTAT3 among all Aldh1l1-eGFP+/S100β+ astrocytes in areas less than 300 μm distant from the tumor, in areas more than 300 μm from the tumor, and in the contralateral hemisphere (Fig. 3a-e). Few astrocytes (0.95% ± 0.19%) were pSTAT3+ in the contralateral hemisphere. In GBM22-bearing brains, we observed a gradient with almost one fifth of all astrocytes labeled for pSTAT in astrocytes less than 300 μm from the tumor (18.66% ± 1.82%)(Fig. 3a,d). The percentage of pSTAT3+ astrocytes gradually decreased with distance from the

tumor as only 5.35% ± 1.01% were pSTAT3+ (Fig. 3c). More than half of the astrocytes within 600 μm of a D54 glioma were pSTAT3+ (Fig. 3b,e) (GBM one-way ANOVA, p-value < 0.0001; Bonferroni's multiple comparison test: peritumoral vs < 300 μm from glioma p-value < 0.0001, peritumoral vs > 300 μm p-value = n. s., < 300 μm from glioma vs > 300 μm from glioma p-value < 0.0001. D54 one-way ANOVA p-value 0.0003, Tukey multiple comparison test: peritumoral vs < 300 μm from glioma p-value = 0.0004, peritumoral vs > 300 μm p-value = 0.0006, < 300 μm from glioma vs > 300 μm from glioma p-value = n. s.).

Sox9 is a transcription factor expressed almost exclusively in astrocytes outside of neurogenic zones of the adult human and mouse brain and is upregulated in reactive astrocytes in models of amyotrophic lateral sclerosis (ALS), Parkinson's Disease, and stroke (Choi et al., 2018; Sun et al., 2017). However, we did not detect an upregulation of Sox9 expression in reactive astrocytes in close proximity or distal to the GBM22 tumor when compared to the contralateral hemisphere (Fig. 3f). In contrast, some scar-forming astrocytes directly at the tumor border, characterized by a reduction in the fine processes and thickened and elongated main processes, lacked Sox9 expression (Fig. 3f, middle). Astrocytes that maintained a branched morphology clearly labeled for Sox9. Those astrocytes were often hypertrophic with enlarged cell bodies and nuclei (Fig. 3f, right). In the contralateral hemisphere, we did not detect Alh1l1-eGFP-positive cells that were negative for Sox9. However, we detected Aldh1l1-eGFP-negative cells positive for Sox9 (Fig. 3f, left). Similarly, we found Sox9+ and Sox9− astrocytes identified by S100β+ in the vicinity of D54 tumors (Fig. 3g). Interestingly, GBM22 human glioma cells expressed Sox9 homogeneously across the tumor while D54 glioma cells were Sox9− (Fig. 3 f-g).

Sox9 has a role in cell proliferation in some cell types (Pritchett et al., 2011) and astrocyte proliferation occurs preferentially at a juxtavascular position after injury (Bardehle et al., 2013). We thus asked whether Sox9-expression levels might be dependent on the vicinity of astrocytes to the vasculature. However, we found both Sox9+ and Sox9− Aldh1l1-eGFP astrocytes directly adjacent to blood vessels (Fig. 3h).

3.3. Peritumoral astrocytes proliferate but do not appear neurotoxic

While astrocytes in the adult uninjured cortical gray matter are post-mitotic, a subset of astrocytes re-enter the cell cycle after focal acute brain injury. To assess if peritumoral astrocytes proliferate, brain tissue from GBM22 tumor or sham Aldh1l1-eGFP-scid mice was stained using an antibody against the proliferation marker Ki67 (Fig. 4a). The percentage of Aldh1l1-eGFP+/Ki67+ double-positive astrocytes among all Aldh1l1-eGFP+ astrocytes was quantified. As expected, no double-positive cells were found in Sham animals while almost 10% of peritumoral astrocytes were actively proliferating at 2–3 weeks after inoculation with glioma cells. A small number of proliferating astrocytes was observed in the contralateral hemisphere (Fig. 4b). Despite astrocyte proliferation, cell numbers surrounding GBM22 tumors did not significantly change (Fig. 4c) and we did not detect Aldh1l1-eGFP + astrocytes positive for the apoptosis marker activated Caspase 3, although we occasionally observed labeled GBM22 or D54 tumor cells indicating that the staining worked (Fig. 4d). This suggests either that GBM22 and D54 tumors did not induce astrocyte cell death or that we were unable to capture astrocyte cell death with this technique.

We next determined if peritumoral astrocytes labeled positive for C3d, a marker that was previously characterized as marker of “neurotoxic” astrocytes (Clarke et al., 2018; Liddelow et al., 2017). We used two different antibodies (see reference in Table 1). While we occasionally observed C3d + cells within the GBM22 tumor mass, Aldh1l1-eGFP + astrocytes within, close to, or farther away from the tumor mass did not co-label for C3d with either of the antibodies used (Fig. 4d).

In summary, D54 and GBM22 glioma growth induced pronounced scar-formation of astrocytes directly adjacent to the tumor. These astrocytes were characterized by morphological changes, increased expression of phosphorylated STAT3 and GFAP, and a subset proliferated. Some of the scar-forming astrocytes lacked Sox9 expression. Their cell bodies and processes were hypertrophied and elongated. Astrocytes in subsequent rows were activated as well, yet their morphology was changed to a lesser degree, and fewer astrocytes labeled positive for pSTAT3 in GBM22 but not D54, while all expressed Sox9.

3.4. Potassium uptake is reduced in peritumoral astrocytes

Several studies have shown that reactive astrocytes display impaired astrocytic potassium and glutamate homeostasis contributing to neuronal hyperexcitability and seizures (Ortinski et al., 2010; Robel et al., 2015). Yet, astrogliosis is a heterogeneous process and functional changes can vary dependent on the disease context and distance to the site of injury (Burda and Sofroniew, 2014). To elucidate if reactive astrocytes surrounding tumors are impaired in function contributing to the enhanced excitatory drive causing tumor-associated epilepsy, we used a combination of RNAScope, immunohistochemistry, western blot, and electrophysiological recordings to assess whether potassium and glutamate uptake is intact.

Whole-cell patch clamp recordings from astrocytes in Aldh1l1-eGFP-scid mice 0–500 μm distant from the GBM22 tumor border or in controls were performed in acute brain slices. Cell capacitance, which correlates with cell size, was unchanged (control C = 15.33 ± 1.13 pF n = 29; peritumoral astrocytes C = 13.54 ± 1.26 pF n = 36; two-tailed Mann-Whitney test, p = 0.0687) suggesting that although astrocyte cell bodies appeared enlarged close to the tumor, the loss of peripheral processes resulted in a lack of net increase of the membrane surface (Fig. 2b and c, 5f, 6g, 7g). This differs from hypertrophied reactive astrocytes without obvious morphological changes, which display an increased cell capacitance, suggesting that their membrane surface is enlarged compared to controls (Robel et al., 2015).

Astrocytic potassium (K^+) conductance is mediated by the barium-sensitive potassium channel Kir4.1 (Olsen and Sontheimer, 2008), which is thought to be responsible for the resting membrane potential (RMP) of astrocytes, averaging around −80 mV. While most of the astrocytes that were recorded in the vicinity of the tumor had a RMP comparable to control astrocytes, a subset of cells was notably depolarized. These cells were often very close to the tumor, were enlarged and had elongated main processes. The average RMP (Fig. 5a) was slightly but significantly reduced in peritumoral astrocytes (RMP = −73.96 ± 0.68 mV n = 107) when compared to control astrocytes (control RMP = −76.22 ± 0.44 mV n = 52; two-tailed Mann Whitney test, p = 0.0396).

To directly assess K^+-uptake, we challenged astrocytes in tumor-bearing and control acute brain slices with pressure applied K^+ (125 mM KCl), which induced an inward current under voltage-clamp conditions (Fig. 5b). The number of ions that moved across the membrane can be determined from the charge transfer, i.e. the area of the Ba^{2+}-sensitive current induced by the puff. There was a decrease in the number of K^+ ions moving across the membrane in peritumoral compared to control astrocytes (control 1.64 ± 0.25 fmol K+, n = 12; peritumoral astrocytes 0.78 ± 0.14, n = 24, two-tailed unpaired *t*-test, p = 0.0022 (Fig. 5b and c).

We next performed RNA, immunohistochemical and Western blot analyses to determine whether Kir4.1 RNA and protein levels were changed in tissue surrounding GBM22. We used fluorescent in situ hybridization (RNAScope) with probes detecting KCNJ10, the gene encoding Kir4.1, to determine if KCNJ10 transcript copy numbers might differ in astrocytes depending on distance to the tumor. We found that transcript density was reduced in peritumoral areas (0–300 μm from the tumor border) compared to contralateral areas in GBM22 tumor animals (Fig. 5d and e). However, total Kir4.1 protein expression as determined by Western blot analysis was increased in peritumoral tissue collected 0–500 μm from the tumor boundary (Fig. 5f and g; relative expression levels of GBM22 peritumoral tissue normalized to GAPDH: contralateral 1.2 ± 0.2 n = 6; peritumoral 2.7 ± 0.5 n = 6, two-tailed paired *t*-test p = 0.0301).

Given the pronounced changes in astrocyte morphology at the tumor border (Figs. 2-4), we next used immunohistochemistry to determine if Kir4.1 protein mislocalization might account for reduced K+ uptake. We noted areas of low and high Kir4.1 signal intensity surrounding the GBM22 and D54 tumors (Fig. 5h and i). Mean Kir4.1 gray value intensities were measured in regions of interest (ROI) in 100 μm increments 0–400 μm from the GBM22 and D54 tumor border. Kir4.1 Signal intensity measurements did not indicate a clear and consistent gradient, which is reflected in the lack of a significant average change in Kir4.1 intensity at different distances and a high variability from data point to data point, which confirms our IHC observation of micro-areas devoid of Kir4.1 next to areas with Kir4.1 signal (Fig. 5j and k).

Taken together with the data showing reduced transcript numbers per area, this suggests that, in some small areas surrounding the tumor, KCNJ10/Kir4.1 is reduced or lacking in fine astrocytic processes that normally cover the brain surface. Yet, protein reduction does not occur in consistent concentric circles from the tumor border. Increased total Kir4.1 protein might be due to increased translation from the remaining KCNJ10 transcripts in the Kir4.1-high micro areas (Fig. 5k).

Lastly, we assessed if Kir4.1 deficient areas had reduced neuronal densities. Similar to previous studies (Campbell et al., 2015; Tewari et al., 2018), it appeared that Nissl + cells were reduced in density close to the tumor, an area that also often showed a reduction in Kir4.1 signal, especially in D54 tumor-bearing mice (Fig. 5k, right panel). Other areas with decreased Kir4.1 immunohistochemistry appeared to have regular Nissl densities (Fig. 5k, left panel). This variability may be explained by potential differences in the length of time that neurons were exposed to astrocytes limited in their ability to buffer potassium.

3.5. Glutamate uptake is impaired in peritumoral astrocytes

Two astrocytic glutamate transporters, Glt-1 (EAAT2, Slc1a2) and Glast (EAAT1, Slc1a3) are responsible for the vast majority of glutamate uptake tightly regulating the concentration of this excitatory neurotransmitter in the extracellular space (Danbolt, 2001). We previously showed in a model of genetically-induced astrogliosis that glutamate uptake is impaired in hypertrophic non-proliferative reactive astrocytes (Robel et al., 2015). High extracellular glutamate can lead to neuronal hyperexcitability, seizures and excitotoxicity (Buckingham and Robel, 2013). Previous studies from our lab showed that extracellular glutamate is elevated in acute brain slices of tumor-bearing mice, driving the development of tumor-associated epilepsy (Buckingham et al., 2011) and that brain imaging of patients with glioma demonstrates elevated glutamate (Robert et al. 2015). Under normal conditions, astrocytes are capable of buffering glutamate concentrations comparable or higher than those measured in the extracellular space of glioma-bearing mice (Yao et al., 2014; Ye and Sontheimer, 1998).

To determine if peritumoral reactive astrocytes impaired in glutamate uptake are contributing to increased levels of extracellular glutamate, we compared the magnitude of glutamate uptake in control and peritumoral astrocytes. Whole-cell patch-clamp recordings from eGFP + astrocytes were performed in acute brain slices from tumor-bearing or control Aldh1l1-eGFP-scid mice. High glutamate concentrations (200 μM) were applied extracellularly using a puffing pipette, and uptake currents were recorded in peritumoral and control astrocytes while blocking K^+ uptake with $BaCl_2$, and neuronal activity with TTX, D-AP5, bicuculline, and $CdCl_2$. Recordings were repeated after blocking glutamate transporters with the inhibitors TBOA and DHK (Fig. 6a). The amount of glutamate taken up was calculated from the TBOA/DHK-sensitive component of the area under the curve and was significantly reduced in peritumoral astrocytes (Fig. 6b) (control 1.813 ± 0.45 fmol glutamate, $n = 20$; peritumoral 0.1306 ± 0.1333, $n = 17$, Mann-Whitney test, $p < 0.0001$).

We next performed immunohistochemical and Western blot analyses to determine whether Glt-1 and Glast protein levels were changed. In protein lysates from peritumoral tissue collected 0–500 μm from the tumor boundary, neither Glt-1 nor Glast levels were changed when compared to the contralateral hemisphere (Fig. 6c-f, 5 μg Glt-1 relative expression levels of GBM22 peritumoral tissue normalized to GAPDH: contralateral 1.1 ± 0.1 n = 6; peritumoral 0.9 ± 0.1 n = 6, two-tailed paired *t*-test p = 0.2136; 10 μg Glast relative expression levels of GBM22 peritumoral tissue normalized to GAPDH: contralateral 0.9 ± 0.2 n = 6; peritumoral 0.9 ± 0.5 n = 6, two-tailed paired *t*-test p = 0.7807). Using immunohistochemistry, no obvious differences in Glt-1 intensity was noted in astrocytes adjacent to the tumor. Yet, astrocytes within the tumor mass appear to have lost their fine processes and Glt-1 expression within those (Fig. 6g). Glast appeared upregulated within the soma and main processes of scar-forming astrocytes directly facing the tumor (Fig. 6g).

These data suggest functional impairment of glutamate uptake by peritumoral astrocytes is likely due to changes in localization of glutamate transporter or lack of fine astrocytic processes. The unchanged overall Glt-1 and Glast expression levels highlight the importance of assessing function of these transporters rather than relying on Western blot data as a proxy for glutamate uptake.

3.6. Glutamine synthetase function is impaired in peritumoral astrocytes

Under physiological rates of activity, the inhibitory synaptic function of GABAergic neurons depends on intra-terminal glutamate. After synaptic release, glutamate is taken up by astrocytes and converted to glutamine by the astrocytic enzyme glutamine synthetase (GS). Glutamine is then released by astrocytes into the extracellular space. The glutamate-glutamine cycle is necessary and rate limiting for the synthesis of the inhibitory neurotransmitter gamma-aminobutyric acid (GABA) by inhibitory neurons (Ortinski et al., 2010). We previously demonstrated a reduced inhibitory drive in peritumoral neurons (Campbell et al., 2015), and defective glutamine synthetase function results in a lack of inhibition resulting in hippocampal hyperexcitability after virally induced astrogliosis (Ortinski et al., 2010) Thus, we next asked if astrocyte-dependent synthesis of the GABA precursor glutamine was disrupted in peritumoral reactive astrocytes.

To determine if peritumoral glutamine production was altered to affect inhibitory tone, slices were incubated in Methionine sulfoximine (MSO) (1.5 mM) for at least 90 min to block glutamine synthetase activity. To generate physiological rates of inhibitory activity observed during behavioral states (Bartos et al., 2002; Klausberger et al., 2003), we used a repetitive train stimulation protocol. Following baseline recordings (0.05 Hz), we elicited a train of four pulses of 50-Hz trains repeated at 20 s intervals for 15 min in peritumoral and control neurons. In the presence of MSO, evoked Inhibitory Postsynaptic Current (eIPSC) peak amplitude decreased significantly more in control compared to peritumoral neurons following the train stimulation protocol (Sham: 56.44 ± 2.49%, n = 6 vs peritumoral: 79.96 ± 7%, n = 8 of pre-train stimulation amplitude respectively, p = 0.002, Fig. 7a and b). This suggests that glutamine supply from astrocytes impaired reloading of GABA during high rates of activity in sham neurons. In peritumoral neurons, such pronounced difference between eIPSC peak amplitudes before and after MSO was not observed (Fig. 7a and b) indicating that peritumoral neurons were impaired in glutamine synthetase function even before MSO application. To test this hypothesis, we exogenously applied glutamine (10 mM, 15 min) to the ACSF to bypass the astrocytic supply of glutamine before evoking IPSCs, followed by the train stimulation. Application of glutamine in peritumoral neurons significantly increased the post-train amplitude of eIPSCs (37 ± 7% of pre-burst stimulation amplitude, p = 0.03, n = 6, Fig. 7c and d). In the presence of glutamine, the amplitude of eIPSCs during the train also increased (Fig. 7d). This result suggests that peritumoral astrocyte-dependent glutamine production is altered and exogenous application of glutamine can restore the associated decrease in inhibitory synaptic function.

To determine if diminished glutamine synthetase function resulted from reduced expression of this enzyme, we performed Western blot analysis. No significant changes in glutamine synthetase protein levels were observed in GBM22 peritumoral cortex compared to the contralateral hemisphere (Fig. 7e and f, relative expression levels of 5 μg GBM22 peritumoral tissue normalized to tubulin: contralateral 0.9 ± 0.15 n = 6; peritumoral 0.8 ± 0.03 n = 6, two-tailed paired *t*-test p = 0.6018). Despite unchanged overall glutamine synthetase levels, scar-forming astrocytes adjacent to GBM22 tumors displayed striking loss of the enzyme in their fine processes and redistribution into the swollen cell body and main processes (Fig. 7g). Interestingly, this was in contrast to immunohistochemistry performed

in D54-inoculated brains. Here, peritumoral astrocytes appeared to have hugely increased overall GS levels (data not shown). Levels are also highest in the soma and main processes (Fig. 7g). Future studies will determine if different glioma types affect astrocyte GS function in variable ways.

In summary, in astrocytes surrounding GBM22, glutamine production was impaired due to changes in glutamine synthetase location and likely exacerbated by the lack of glutamate uptake into peritumoral astrocytes resulting in both an enhanced excitatory drive due to elevated extracellular glutamate (Buckingham et al., 2011) and the decreased activity of inhibitory interneurons (Fig. 7 and (Campbell et al., 2015)) which was rescued by exogenous application of glutamine. These data point to a crucial role for astrocytes in offsetting the balance between neuronal inhibition and excitation in tumor-associated epilepsy.

4. Discussion

For more than a decade, astrocytes have been implicated in epilepsy and evidence of their causative role in epilepsy and many other neurological diseases is mounting (Liddelow et al., 2017; Rothstein, 1995; Tong et al., 2014). Glioma is distinct from other inducers of acquired epilepsies such as trauma or stroke given the bidirectional dynamic signaling that brain and glioma cells exert on each other (Cuddapah et al., 2014; Rosati et al., 2009). Here, we asked if astrocytes surrounding glioma lose their homeostatic functions and if this astrocyte response is different from astrocyte dysfunction in other neurological diseases.

4.1. Scar-formation and epilepsy

Similar to other focal injuries (Burda et al., 2015; Sofroniew, 2009), we found that glioma induced morphologically and molecularly distinct types of reactive astrocytes. In contrast to the gradient of severity of astrocyte changes that depends on the distance to focal injury, molecular changes in peritumoral astrocytes was variable. The glial scar surrounding a glioma is highly dynamic given the constant growth of the tumor, unlike the permanent and stable glial scar that forms after other types of focal injury (Fig. 8).

Within the glioma-bearing hemisphere but > 500 μm distant from the tumor border, most astrocytes were moderately reactive and appeared relatively homogeneous in morphology and expression levels of intermediate filaments. These astrocytes were pSTAT3-negative in GBM22, Sox9-positive, did not proliferate, and lacked elongated processes. About half of the astrocytes > 500 μm distant from the D54 tumor border were pSTAT3-positive but otherwise similar to GBM22 peritumoral astrocytes distant from the tumor.

Variability was observed of the reactive changes in astrocytes in direct vicinity of a glioma. Astrocytes at the tumor border either formed a scar or appeared more similar to moderately reactive astrocytes, presumably when they were exposed to glioma cells for a shorter period of time.

Scar-forming astrocytes directly at the glioma border had pronounced elongation of their main processes. Finer processes appeared reduced in density based on reporter labeling in Aldh1l1-eGFP-scid GBM22 mice and lack of expression of other membrane-associated

proteins including Glt-1, Glast, and Kir4.1. Elongated processes were either oriented perpendicular to the tumor mass or appeared to run along the tumor border. One fifth (GBM22) to about half (D54) of the astrocytes within this area were positive for pSTAT3 and about 10% of astrocytes at the tumor border proliferated.

Penetrating brain injury, spinal cord injury or stroke induce similar scar formation. Here, pSTAT3-positive, proliferating, and “palisading” astrocytes form long thickened processes that perpendicularly orient toward the injury and finer processes can be lost (Oberheim et al., 2008; Robel et al., 2011; Sun et al., 2017; Wanner et al., 2013). Interestingly, Oberheim et al. correlated such morphological changes in astrocytes with seizure development in different models of epilepsy (Oberheim et al., 2008). Fine astrocyte processes are part of the tripartite synapse and enwrap ~100,000 synapses within a single astrocyte domain. It is thus likely that the loss of astrocyte complexity as observed in scar-forming astrocytes causes spill-over of neurotransmitters or reduced potassium-uptake as observed in our study, which can contribute to hyperexcitability.

Other studies report that the transcription factor Sox9 increases in reactive astrocytes in amyloid lateral sclerosis (ALS), a mouse model of stroke, and in Parkinson's Disease (Choi et al., 2018; Sun et al., 2017). Interestingly, Sox9 expression was varied in peritumoral astrocytes. Astrocytes close to a tumor, which still had a bushy morphology and appeared hypertrophic but not elongated, expressed Sox9. Yet, scarforming astrocytes, which had lost their finer processes, sometimes lacked the transcription factor Sox9 (GBM22 and D54, yet less frequent in D54). This loss of Sox 9 is possibly unique to peritumoral astrocytes. However, previous studies do not show high resolution microscopy of astrocytes at lesion sites, nor do they quantify the portion of reactive astrocytes expressing Sox9, which makes it difficult to judge whether indeed all reactive astrocytes express Sox9 in the context of ALS, stroke, or Parkinson's Disease.

Thus, for future studies, Sox9 might be informative in determining the “age” of the tumor-astrocyte border with Sox9-positive astrocytes interfacing with a newly grown tumor and astrocytes losing Sox9 after they have been exposed to the tumor for longer periods of time.

4.2. Potassium uptake, resting membrane potential and cell proliferation

The loss of Kir4.1 function is pathologically relevant and associated with other forms of epilepsy and neurological disorders that present with seizures. To name but a few, in Huntington's disease, reduced expression and function of the Kir4.1 potassium channel even in the absence of astrogliosis is associated with impaired medium spiny neuron function (Tong et al., 2014) and in a murine model of the neurodevelopmental disorder Rett syndrome, Kir4.1 expression and barium-sensitive Kir4.1 currents were decreased (Kahanovitch et al., 2018).

We found that peritumoral astrocytes were functionally more severely impaired than our previous results indicated in a mouse with genetically induced astrogliosis, which caused spontaneous recurrent seizures (Robel et al., 2015). In this model, astrocytes are clearly hypertrophic and positive for many astrogliosis markers, yet do not enter the cell cycle or form scars, and potassium uptake and resting membrane potential (RMP) were intact

(Robel et al., 2009). Mature astrocytes in the healthy adult brain and spinal cord have a resting membrane potential of −85mV, which is close to the K^+ equilibrium potential and established by Kir4.1 (Olsen et al., 2007; Olsen and Sontheimer, 2008). GBM22 and D54 peritumoral reactive astrocytes had lower average RMPs with a subset of astrocytes being notably depolarized and a reduced K^+ uptake capacity when compared to control astrocytes.

An interesting link between Kir4.1 expression levels, the resting membrane potential, and a cell's capacity to proliferate exists. During postnatal development, murine glial progenitors continue to divide for about one week before they exit the cell cycle and mature. Dividing cells have resting membrane potentials of −30 to −50mV, relatively positive when compared to differentiated cells (MacFarlane and Sontheimer, 1997; Sontheimer et al., 1989). Astrocyte maturation is correlated to cell-cycle exit associated with a negative shift in resting potential and the upregulation of Kir4.1, which is expressed strongly in all brain regions by postnatal day 30 (Nwaobi et al., 2014). After injury, it has been difficult to directly correlate ion channel function with proliferation at a single cell level in situ, as only a subpopulation of reactive astrocytes re-enters the cell cycle. Surrounding glioma, ~10% of peritumoral astrocytes were actively proliferating, which is comparable to other models of focal brain injury (Bardehle et al., 2013). Whether the proliferation of reactive astrocytes is a potentially beneficial reaction of the injured brain trying to repair itself or a side effect of the downregulation of Kir channels and thus the passive acquisition of immature properties remains to be determined.

The relationship between astrocytes' ability to buffer potassium and maintain a RMP close to the K^+ equilibrium potential and their lack of proliferation appears to be consistent with our finding that non-proliferative, non-elongated reactive astrocytes with unchanged RMP (in a mouse model of astrogliosis (Robel et al., 2015)) are capable of taking up K^+, while proliferative scar-forming astrocytes surrounding a glioma had a lower RMP and were impaired in their ability to uptake K^+. As noted above, the reduced morphological complexity of scarforming astrocytes, which resulted in less area covered with Kir4.1 despite increased total protein levels, might account for both impaired potassium uptake and reduced membrane potentials.

Another recent study demonstrated disturbed potassium homeostasis in the context of glioma. The authors found increased expression of the voltage-sensitive potassium channel Kv1.3 in astrocytes and microglia surrounding G1261 gliomas. Kv1.3 opens upon membrane depolarization, facilitating K^+ release. Pharmacological inhibition of Kv1.3 improved neuronal survival in G1261 glioma-bearing mice, possibly through restoration of Glt-1 function (Grimaldi et al., 2018).

4.3. Abnormal glutamate homeostasis affects excitation and inhibition

Glt-1 function is closely linked to glioma growth, and this is corroborated by a study using the β-lactam antibiotic thiamphenicol to increase glutamate transporter expression levels. This correlated with increased numbers of peritumoral neurons, decreased tumor growth, and better survival in a rat model of glioma (Sattler et al., 2013). Glutamate and potassium homeostasis are linked, given the electrogenic nature of the glutamate transporters Glt-1 and Glast (Zhou and Danbolt, 2013) that requires an electrochemical gradient of potassium

and a very negative resting membrane potential for efficient function. We demonstrated that astrocyte potassium uptake is reduced, likely contributing to increased extracellular potassium concentrations alongside Kv1.3 (Grimaldi et al., 2018) and a notably depolarized resting membrane potential, both of which are detrimental to glutamate transporter function. Additionally, a reduction in fine astrocytic processes might affect the cell's ability to uptake glutamate. Indeed, after the extracellular application of glutamate, glutamate uptake currents were reduced, providing direct functional evidence for impaired glutamate uptake in peritumoral astrocytes.

In glioma patients with tumor-associated epilepsy, glutamine synthetase, an astrocytic enzyme important for proper processing of glutamate, was significantly reduced in expression when compared to non-epileptic GBM individuals (Rosati et al., 2009). We found that glutamine synthetase, although expressed, is redistributed away from the membrane into the astrocyte cell body and main processes, resulting in failure to provide the GABA-precursor glutamine to inhibitory interneurons similar to previous results in virally induced astrogliosis (Ortinski et al., 2010). This led to reduced eIPSCs further contributing to the imbalance between inhibition and excitation (Buckingham et al., 2011; Campbell et al., 2014).

Impaired glutamate homeostasis is, in fact, commonly associated with seizure disorders. A decrease in glutamate uptake is characterized astrocytes in a model of focal cortical dysplasia, a neurodevelopmental disorder presenting with seizures (Campbell et al., 2014). In models of Rett syndrome or Alexander Disease, glutamate transporter transcripts were reduced and glutamate clearance was abnormal (Okabe et al., 2012) or abolished (Minkel et al., 2015; Tian et al., 2010).

5. Conclusions

In conclusion, we suggest that scar-forming peritumoral astrocytes are severely impaired in their ability to maintain potassium and glutamate homeostasis. This contributes to elevated extracellular glutamate and potassium concentrations, as well as decreased levels of the GABA precursor glutamine, which resulted in decreased inhibition. Dysfunction of peritumoral astrocytes is thus a likely contributor to tumor-associated epilepsy.

Acknowledgments

We are grateful to Kijana George for assistance with data analysis. We'd like to thank Paul Youmans and Miki Jinno for technical assistance and maintenance of the mouse colonies. Antibodies against glutamate transporters were a gift from Niels Danbolt, University of Oslo. We are grateful to Aubrey Phares for proofreading the manuscript. The authors state no conflict of interests.

Funding

Funding was provided by the National Institutes of Health (NIH) RO1 NS036692 (HS), RO1 NS082851 (HS), RO1 NS052634 (HS), RO1 NS105807 (SR). SR was also supported by the Epilepsy Foundation and the American Brain Tumor Association (ABTA).

Abbreviations:

ACSF	artificial cerebral spinal fluid

AED	Anti-epileptic drugs
CNS	Central nervous system
eIPSC	evoked Inhibitory Postsynaptic Current
GFAP	glial fibrillary acidic protein
MSO	methionine sulfoximine
PFA	paraformaldehyde
RMP	resting membrane potential
TBOA	DL-threo-β-Benzyloxyaspartic acid
TTX	tetrodotoxin

References

Choi D, Eun J, Kim B, Jou I, Park S, Joe E, 2018. A Parkinson's disease gene, DJ-1, repairs brain injury through Sox9 stabilization and astrogliosis. Glia 66, 445–458. 10.1002/glia.23258. [PubMed: 29105838]

Anderson MA, Burda JE, Ren Y, Ao Y, O'Shea TM, Kawaguchi R, Coppola G, Khakh BS, Deming TJ, Sofroniew MV, 2016. Astrocyte scar formation aids central nervous system axon regeneration. Nature 532. 10.1038/nature17623.

Bardehle S, Krüger M, Buggenthin F, Schwausch J, Ninkovic J, Clevers H, Snippert HJ, Theis FJ, Meyer-Luehmann M, Bechmann I, Dimou L, Götz M, 2013. Live imaging of astrocyte responses to acute injury reveals selective juxta-vascular proliferation. Nat. Neurosci 16. 10.1038/nn.3371.

Bartos M, Vida I, Frotscher M, Meyer A, Monyer H, Geiger JR, Jonas P, 2002. Fast synaptic inhibition promotes synchronized gamma oscillations in hippocampal interneuron networks. Proc. Natl. Acad. Sci 99, 13222–13227. 10.1073/pnas.192233099. [PubMed: 12235359]

Bedner P, Dupper A, Hüttmann K, Müller J, Herde M, 2015. Astrocyte uncoupling as a cause of human temporal lobe epilepsy. Brain: J. Neurol 138, 1208–1222. 10.1093/brain/awv067.

Brenner M, Johnson A, Boespflug-Tanguy O, Rodriguez D, Goldman J, Messing A, 2001. Mutations in GFAP, encoding glial fibrillary acidic protein, are associated with Alexander disease. Nat. Genet 27, 117–120. 10.1038/83679. [PubMed: 11138011]

Buckingham SC, Robel S, 2013. Glutamate and tumor-associated epilepsy: glial cell dysfunction in the peritumoral environment. Neurochem. Int 63, 696–701. 10.1016/j.neuint.2013.01.027. [PubMed: 23385090]

Buckingham SC, Campbell SL, Haas BR, Montana V, Robel S, Ogunrinu T, Sontheimer H, 2011. Glutamate release by primary brain tumors induces epileptic activity. Nat. Med 17, 1269–1274. 10.1038/nm.2453. [PubMed: 21909104]

Burda JE, Sofroniew MV, 2014. Reactive gliosis and the multicellular response to CNS damage and disease. Neuron 81, 229–248. 10.1016/j.neuron.2013.12.034. [PubMed: 24462092]

Burda JE, Bernstein AM, Sofroniew MV, 2015. Astrocyte roles in traumatic brain injury. Exp. Neurol 275. 10.1016/j.expneurol.2015.03.020.

Bush TG, Puvanachandra N, Horner CH, Polito A, Ostenfeld T, Svendsen CN, Mucke L, Johnson MH, Sofroniew MV, 1999. Leukocyte infiltration, neuronal degeneration, and neurite outgrowth after ablation of scar-forming, reactive astrocytes in adult transgenic mice. Neuron 23, 297–308. 10.1016/s0896-6273(00)80781-3. [PubMed: 10399936]

Campbell SL, Hablitz JJ, Olsen ML, 2014. Functional changes in glutamate transporters and astrocyte biophysical properties in a rodent model of focal cortical dysplasia. Front. Cell. Neurosci 8, 425. 10.3389/fncel.2014.00425. [PubMed: 25565960]

Campbell SL, Robel S, Cuddapah VA, Robert S, Buckingham SC, Kahle KT, Sontheimer H, 2015. GABAergic disinhibition and impaired KCC2 cotransporter activity underlie tumor-associated epilepsy. Glia 63, 23–36. 10.1002/glia.22730. [PubMed: 25066727]

Clarke LE, Liddelow SA, Chakraborty C, Münch AE, Heiman M, Barres BA, 2018. Normal aging induces A1-like astrocyte reactivity. Proc. Natl. Acad. Sci 115, 201800165. 10.1073/pnas.1800165115.

Cuddapah V, Robel S, Watkins S, Sontheimer H, 2014. A neurocentric perspective on glioma invasion. Nat. Rev. Neurosci 15, 455–465. 10.1038/nrn3765. [PubMed: 24946761]

Danbolt NC, 2001. Glutamate uptake. Prog. Neurobiol 65, 1–105. 10.1016/S0301-0082(00)00067-8. [PubMed: 11369436]

Faulkner JR, Herrmann JE, Woo MJ, Tansey KE, Doan NB, Sofroniew MV, 2004. Reactive astrocytes protect tissue and preserve function after spinal cord injury. J. Neurosci 24, 2143–2155. 10.1523/jneurosci.3547-03.2004. [PubMed: 14999065]

Giannini C, Sarkaria JN, Saito A, Uhm JH, Galanis E, Carlson BL, Schroeder MA, James DC, 2005. Patient tumor EGFR and PDGFRA gene amplifications retained in an invasive intracranial xenograft model of glioblastoma multiforme. Neuro Oncol. 7, 164–176. 10.1215/s1152851704000821. [PubMed: 15831234]

Grimaldi A, D'Alessandro G, Castro M, Lauro C, Singh V, Pagani F, Sforna L, Grassi F, Angelantonio S, Catacuzzeno L, Wulfif H, Limatola C, Catalano M, 2018. Kv1.3 activity perturbs the homeostatic properties of astrocytes in glioma. Sci Rep-uk 8, 7654. 10.1038/s41598-018-25940-5.

Herrmann JE, Imura T, Song B, Qi J, Ao Y, Nguyen TK, Korsak RA, Takeda K, Akira S, Sofroniew MV, 2008. STAT3 is a critical regulator of astrogliosis and scar formation after spinal cord injury. J. Neurosci 28, 7231–7243. 10.1523/jneurosci.1709-08.2008. [PubMed: 18614693]

Holmseth S, Dehnes Y, Bjørnsen LP, Boulland J-L, Furness DN, Bergles D, Danbolt NC, 2005. Specificity of antibodies: Unexpected cross-reactivity of antibodies directed against the excitatory amino acid transporter 3 (EAAT3). Neuroscience 136, 649–660. 10.1016/j.neuroscience.2005.07.022. [PubMed: 16344142]

Kahanovitch U, Cuddapah VA, Pacheco NL, Holt LM, Mulkey DK, Percy AK, Olsen ML, 2018. MeCP2 Deficiency Leads to Loss of Glial Kir4.1. Eneuro 5. 10.1523/eneuro.0194-17.2018. ENEURO.0194-17.2018.

Kimbrough IF, Robel S, Roberson ED, Sontheimer H, 2015. Vascular amyloidosis impairs the gliovascular unit in a mouse model of Alzheimer's disease. Brain 138, 3716–3733. 10.1093/brain/awv327. [PubMed: 26598495]

Klausberger T, Magill PJ, Márton LF, Roberts DJ, Cobden PM, Buzsáki G, Somogyi P, 2003. Brain-state- and cell-type-specific firing of hippocampal interneurons in vivo. Nature 421, 844–848. 10.1038/nature01374. [PubMed: 12594513]

Kurzwelly D, Herrlinger U, mon, 2010. Seizures in patients with low-grade gliomas–incidence, pathogenesis, surgical management, and pharmacotherapy. Adv. Tech. Stand. Neurosurg 35, 81–111. [PubMed: 20102112]

Li Y, Zhou Y, Danbolt N, 2012. The Rates of Postmortem Proteolysis of Glutamate Transporters Differ Dramatically between Cells and between Transporter Subtypes. J. Histochem. Cytochem 60, 811–821. 10.1369/0022155412458589. [PubMed: 22859703]

Liddelow SA, Guttenplan KA, Clarke LE, Bennett FC, Bohlen CJ, Schirmer L, Bennett ML, Münch AE, Chung W-S, Peterson TC, Wilton DK, Frouin A, Napier BA, Panicker N, Kumar M, Buckwalter MS, Rowitch DH, Dawson VL, wson T, Stevens B, Barres BA, 2017. Neurotoxic reactive astrocytes are induced by activated microglia. Nature 541, 481–487. 10.1038/nature21029. [PubMed: 28099414]

Lynam LM, Lyons MK, Drazkowski JF, Sirven JI, Noe KH, Zimmerman RS, Wilkens JA, 2007. Frequency of seizures in patients with newly diagnosed brain tumors: a retrospective review. Clin. Neurol. Neurosurg 109, 634–638. 10.1016/j.clineuro.2007.05.017. [PubMed: 17601658]

MacFarlane S, Sontheimer H, 1997. Electrophysiological Changes that Accompany Reactive Gliosis in Vitro, vol. 17. pp. 7316–7329.

Maruyama C, Suemizu H, Tamamushi S, Kimoto S, Tamaoki N, Ohnishi Y, 2002. Genotyping the Mouse Severe Combined Immunodeficiency Mutation Using the Polymerase Chain Reaction with

Confronting Two-Pair Primers (PCR-CTPP). vol. 51. Experimental animals/Japanese Association for Laboratory Animal Science, pp. 391–393. [PubMed: 12221933]

Minkel HR, Anwer TZ, Arps KM, Brenner M, Olsen ML, 2015. Elevated GFAP induces astrocyte dysfunction in caudal brain regions: a potential mechanism for hindbrain involved symptoms in type II Alexander disease. Glia 63, 2285–2297. 10.1002/glia.22893. [PubMed: 26190408]

Nwaobi SE, Lin E, Peramsetty SR, Olsen ML, 2014. DNA methylation functions as a critical regulator of Kir4.1 expression during CNS development. Glia 62, 411–427. 10.1002/glia.22613. [PubMed: 24415225]

Oberheim N, Tian G, Han X, Peng W, Takano T, Ransom B, Nedergaard M, 2008. Loss of astrocytic domain organization in the epileptic brain. J. Neurosci 28, 3264–3276. 10.1523/jneurosci.4980-07.2008. [PubMed: 18367594]

Okabe Y, Takahashi T, Mitsumasu C, Kosai K, Tanaka E, Matsuishi T, 2012. Alterations of gene expression and glutamate clearance in astrocytes derived from an MeCP2-null mouse model of Rett syndrome. PLoS One 7, e35354. 10.1371/journal.pone.0035354. [PubMed: 22532851]

Olsen ML, Sontheimer H, 2008. Functional implications for Kir4.1 channels in glial biology: from K+ buffering to cell differentiation. J. Neurochem 107, 589–601. 10.1111/j.1471-4159.2008.05615.x. [PubMed: 18691387]

Olsen M, Campbell S, Sontheimer H, 2007. Differential distribution of Kir4.1 in spinal cord astrocytes suggests regional differences in K+ homeostasis. J. Neurophysiol 98, 786–793. 10.1152/jn.00340.2007. [PubMed: 17581847]

Olsen ML, Higashimori H, Campbell SL, Hablitz JJ, Sontheimer H, 2006. Functional expression of Kir4.1 channels in spinal cord astrocytes. Glia 53, 516–528. 10.1002/glia.20312. [PubMed: 16369934]

Olsen ML, Khakh BS, Skatchkov SN, Zhou M, Lee JC, Rouach N, 2015. New insights on astrocyte ion channels: critical for homeostasis and neuron-glia signaling. J. Neurosci 35, 13827–13835. 10.1523/jneurosci.2603-15.2015. [PubMed: 26468182]

Ortinski PI, Dong J, Mungenast A, Yue C, Takano H, Watson DJ, Haydon PG, Coulter DA, 2010. Selective induction of astrocytic gliosis generates deficits in neuronal inhibition. Nat. Neurosci 13, 584–591. 10.1038/nn.2535. [PubMed: 20418874]

Porter KR, McCarthy BJ, Freels S, Kim Y, Davis FG, 2010. Prevalence estimates for primary brain tumors in the United States by age, gender, behavior, and histology. Neuro Oncol. 12, 520–527. 10.1093/neuonc/nop066. [PubMed: 20511189]

Pritchett J, Athwal V, Roberts N, Hanley NA, Hanley K, 2011. Understanding the role of SOX9 in acquired diseases: lessons from development. Trends Mol. Med 17, 166–174. 10.1016/j.molmed.2010.12.001. [PubMed: 21237710]

Reif PS, Strzelczyk A, Rüegg S, Jacobs AH, Haag A, Hermsen A, Sure U, Knake S, Hamer HM, Strik H, Krämer G, Engenhart-Cabilic R, Rosenow F, 2010. Primare Hirntumoren und Hirnmetastasen. Der Nervenarzt 81, 1467–1475. 10.1007/s00115-010-3011-y. [PubMed: 20495775]

Robel S, 2016. Astroglial scarring and seizures: a cell biological perspective on epilepsy. Neuroscience 23 10.1177/1073858416645498. 1073858416645498 168.

Robel S, Sontheimer H, 2015. Glia as drivers of abnormal neuronal activity. Nat. Neurosci 19, 28. 10.1038/nn.4184.

Robel S, Mori T, Zoubaa S, Schlegel J, Sirko S, Faissner A, Goebbels S, Dimou L, Götz M, 2009. Conditional deletion of β1-integrin in astroglia causes partial reactive gliosis. Glia 57, 1630–1647. 10.1002/glia.20876. [PubMed: 19373938]

Robel S, Bardehle S, Lepier A, Brakebusch C, Götz M, 2011. Genetic deletion of cdc 42 reveals a crucial role for astrocyte recruitment to the injury site in vitro and in vivo. J. Neurosci 31, 12471–12482. 10.1523/jneurosci.2696-11.2011. [PubMed: 21880909]

Robel S, Buckingham SC, Boni JL, Campbell SL, Danbolt NC, Riedemann T, Sutor B, Sontheimer H, 2015. Reactive astrogliosis causes the development of spontaneous seizures. J. Neurosci 35, 3330–3345. 10.1523/jneurosci.1574-14.2015. [PubMed: 25716834]

Robert SM, Buckingham SC, Campbell SL, Robel S, Holt KT, Ogunrinu-Babarinde T, Warren PP, White DM, Reid MA, Eschbacher JM, Berens ME, Lahti AC, Nabors LB, Sontheimer H, 2015.

SLC7A11 expression is associated with seizures and predicts poor survival in patients with malignant glioma, n.d.. Sci. Transl. Med 7 10.1126/scitranslmed.aaa8103. 289ra86–289ra86.

Rosati A, Marconi S, Polio B, Tomassini A, Lovato L, Maderna E, Maier K, Schwartz A, Rizzuto N, Padovani A, Bonetti B, 2009. Epilepsy in glioblastoma multiforme: correlation with glutamine synthetase levels. J. Neuro Oncol 93, 319–324. 10.1007/s11060-008-9794-z.

Ross L, Naduvil AM, Bulacio JC, Najm IM, Gonzalez-Martinez JA, 2018. Stereoelectroencephalography-guided laser ablations in patients with neocortical pharmacoresistant focal epilepsy: concept and operative technique. Oper Neurosurg 30, 1823. 10.1093/ons/opy022.

Rothstein J, 1995. Excitotoxicity and neurodegeneration in amyotrophic lateral sclerosis. Clin. Neurosci 3, 348–359. [PubMed: 9021256]

Sattler R, Tyler B, Hoover B, Coddington LT, Recinos V, Hwang L, Brem H, Rothstein JD, 2013. Increased expression of glutamate transporter GLT-1 in peritumoral tissue associated with prolonged survival and decreases in tumor growth in a rat model of experimental malignant glioma. J. Neurosurg 119, 878–886. 10.3171/2013.6.jns122319. [PubMed: 23909244]

Seifert G, Schilling K, Steinhäuser C, 2006. Astrocyte dysfunction in neurological disorders: a molecular perspective. Nat. Rev. Neurosci 7, 194–206. 10.1038/nrn1870. [PubMed: 16495941]

Shandra O, Winemiller AR, Heithoff BP, Munoz-Ballester C, George K, Benko MJ, Zuidhoek I, Besser MN, Curley DE, Edwards FG, Mey A, Harrington AN, Kitchen JP, Robel S, 2019. Repetitive diffuse mild traumatic brain injury causes an atypical astrocyte response and spontaneous recurrent seizures. J. Neurosci 39, 1944–1963. 10.1523/jneurosci.1067-18.2018. 1067-18. [PubMed: 30665946]

Sofroniew MV, 2009. Molecular dissection of reactive astrogliosis and glial scar formation. Trends Neurosci. 32, 638–647. 10.1016/j.tins.2009.08.002. [PubMed: 19782411]

Sofroniew MV, 2014. Astrogliosis. Csh Perspect Biol 7, a020420. 10.1101/cshperspect.a020420.

Sontheimer H, Perouansky M, Hoppe D, Lux H, Grantyn R, Kettenmann H, 1989. Glial cells of the oligodendrocyte lineage express proton-activated Na+ channels. J. Neurosci. Res 24, 496–500. 10.1002/jnr.490240406. [PubMed: 2557457]

Sun W, Cornwell A, Li J, Peng S, Osorio JM, Aalling N, Wang S, Benraiss A, Lou N, Goldman SA, Nedergaard M, 2017. SOX9 is an astrocyte-specific nuclear marker in the adult brain outside the neurogenic regions. J. Neurosci 37, 4493–4507. 10.1523/jneurosci.3199-16.2017. [PubMed: 28336567]

Tewari BP, Chaunsali L, Campbell SL, Patel DC, Goode AE, Sontheimer H, 2018. Perineuronal nets decrease membrane capacitance of peritumoral fast spiking interneurons in a model of epilepsy. Nat. Commun 9, 4724. 10.1038/s41467-018-07113-0. [PubMed: 30413686]

Tian R, Wu X, Hagemann TL, Sosunov AA, Messing A, McKhann GM, Goldman JE, 2010. Alexander disease mutant glial fibrillary acidic protein compromises glutamate transport in astrocytes. J. Neuropathol. Exp. Neurol 69, 335–345. 10.1097/nen.0b013e3181d3cb52. [PubMed: 20448479]

Tong X, Ao Y, Faas GC, Nwaobi SE, Xu J, Haustein MD, Anderson MA, Mody I, Olsen ML, Sofroniew MV, Khakh BS, 2014. Astrocyte Kir4.1 ion channel deficits contribute to neuronal dysfunction in Huntington's disease model mice. Nat. Neurosci 17, 694–703. 10.1038/nn.3691. [PubMed: 24686787]

Trachtenberg M, Pollen D, 1970. Neuroglia: biophysical properties and physiologic function. Science (New York, N.Y.) 167, 1248–1252.

Wanner IB, Anderson MA, Song B, Levine J, Fernandez A, Gray-Thompson Z, Ao Y, Sofroniew MV, 2013. Glial scar borders are formed by newly proliferated, elongated astrocytes that interact to corral inflammatory and fibrotic cells via STAT3-dependent mechanisms after spinal cord injury. J. Neurosci 33, 12870–12886. 10.1523/jneurosci.2121-13.2013. [PubMed: 23904622]

Watkins S, Robel S, Kimbrough IF, Robert SM, Ellis-Davies G, Sontheimer H, 2014. Disruption of astrocyte-vascular coupling and the blood-brain barrier by invading glioma cells. Nat. Commun 5, 4196. 10.1038/ncomms5196. [PubMed: 24943270]

Wetherington J, Serrano G, Dingledine R, 2008. Astrocytes in the epileptic brain. Neuron 58, 168–178. 10.1016/j.neuron.2008.04.002. [PubMed: 18439402]

Yao P-S, Kang D-Z, Lin R-Y, Ye B, Wang W, Ye Z-C, 2014. Glutamate/glutamine metabolism coupling between astrocytes and glioma cells: neuroprotection and inhibition of glioma growth. Biochem Bioph Res Co 450, 295–299. 10.1016/j.bbrc.2014.05.120.

Ye Z, Sontheimer H, 1998. Glial glutamate transport as target for nitric oxide: consequences for neurotoxicity. Prog. Brain Res 118, 241–251. [PubMed: 9932446]

Zhou Y, Danbolt N, 2013. GABA and glutamate transporters in brain. Front. Endocrinol 4, 165. 10.3389/fendo.2013.00165.

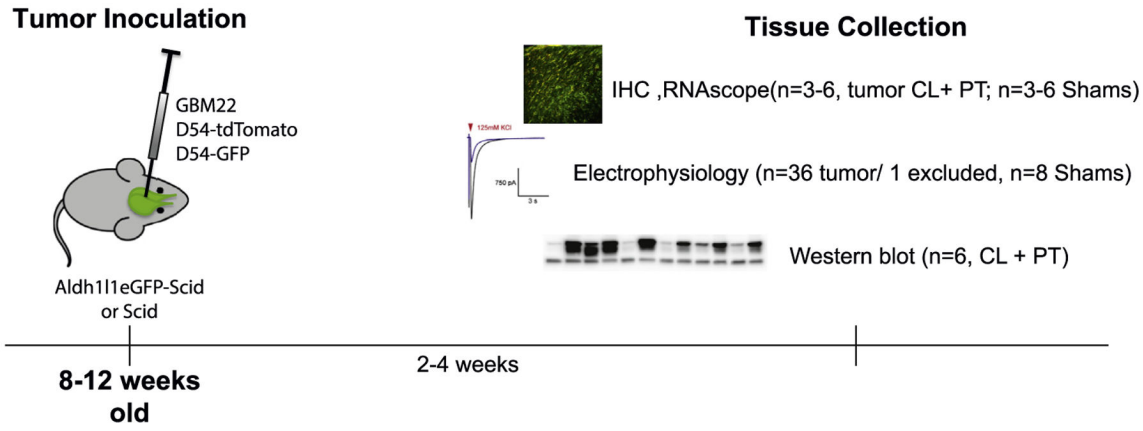

Fig. 1.

Timeline and experimental design. Aldh1l1-eGFP-Scid male and female mice were inoculated with GBM22, D54-GFP or D54-tdTomato at 8–12 weeks of age. Animals were sacrificed 2–4 weeks after inoculation with the exact time based on weight loss, which is indicative of tumor growth. Brains were collected for immunohistochemistry, electrophysiology, RNAScope (fluorescent in situ hybridization) or Western blot analysis.

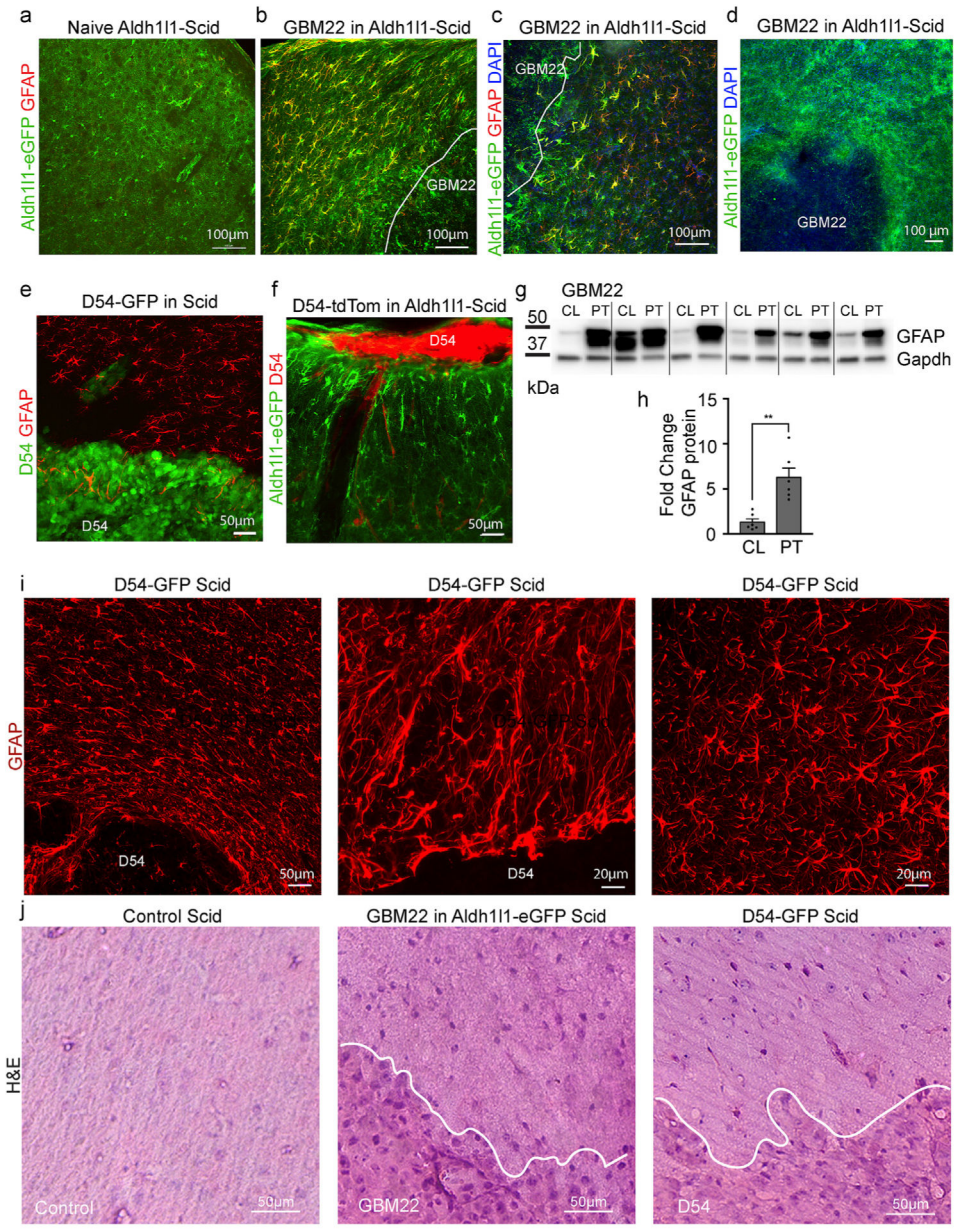

Fig. 2.

Gliomas induce astrogliosis and scar-formation. **a.** Aldh1l1-eGFP-Scid control mice show low or no GFAP expression in the cortical gray matter. **b,c.** Aldh1l1-eGFP-Scid mice injected with GBM22 glioma cells showed widespread astrogliosis around the tumor mass and upregulate the astrogliosis marker GFAP. Collapsed stacks of confocal images of 50 μm slices from PFA-perfused brain tissue. **d.** Confocal image of a 300 μm acute GBM22-bearing Aldh1l1-eGFP brain slice that was fixed in PFA following electrophysiological recordings shows an increase in GFP intensity surrounding the glioma (a,b,c,d n = 6). **e,f.** Similar observations (GFAP upregulation, also see **i.** and enhanced GFP signal in astrocytes adjacent to the tumor) were made when D54-GFP glioma cells were injected (e,f n = 4). **g.** Western blotting for GFAP in control and peritumoral cortex. **h.** GFAP protein levels were

quantified as fold change in protein expression with GAPDH used as a loading control (g,h n = 6). **i.** High magnification images of GFAP labeling in a slice from a D54-tumor bearing animal indicated elongation of astrocytic processes and scar-formation along the tumor border (n = 4). **j.** Hematoxylin & Eosin staining of Shams, GBM22 and D54 tumor-bearing mice (n = 3 in each group).

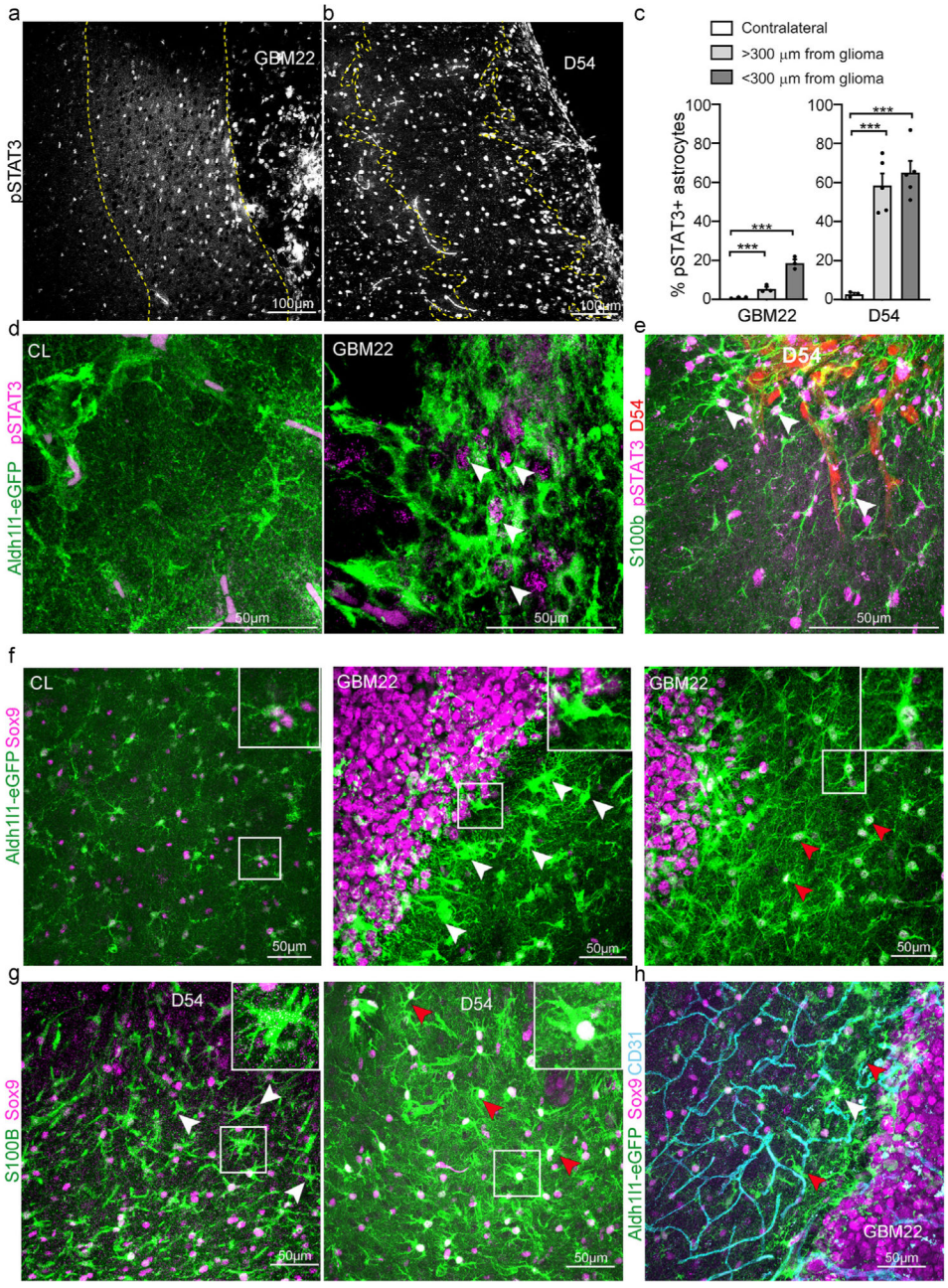

Fig. 3.

Phospho-STAT3 and Sox9 expression patterns in reactive astrocytes at different distances from the tumor. **a.** Confocal images of pSTAT3+ cells in a GBM22 mouse brain slice. **b.** Confocal images of pSTAT3+ cells in a D54 mouse brain slice. Dashed lines define tumor border and distance of 300 μm from the tumor. **c.** Quantitative analysis of pSTAT3-positive astrocytes (Aldh1l1-eGFP in GBM22, S100β in D54) in the peritumoral area 300 μm from the tumor (PT < 300 μm) and in the peritumoral area further than 300 μm from the tumor border (PT > 300 μm) compared to the contralateral area (CL). **d.** Confocal images of Aldh1l1-eGFP + brain slices co-labeled for pSTAT3 in a GBM22 peritumoral area.

Unspecific magenta staining can be detected within blood vessels. **e.** Confocal images of S100β+ brain slices co-labeled for pSTAT3 in a D54 peritumoral area. White arrows point to pSTAT3+ astrocytes. **f,g.** Confocal images of Sox9+ cells in (**f**) an Aldh1l1-eGFP GBM22 or (**g**) D54 brain slice. Red arrows point to Sox9-positive astrocytes. White arrows point to hypertrophic astrocytes lacking Sox9. The white square shows a high magnification view of one of these astrocytes. **h.** Aldh1l1-eGFP GBM22 brain slices co-labeled with Sox9 and the endothelial cell marker CD31. (all panels, n = 3 mice per group).

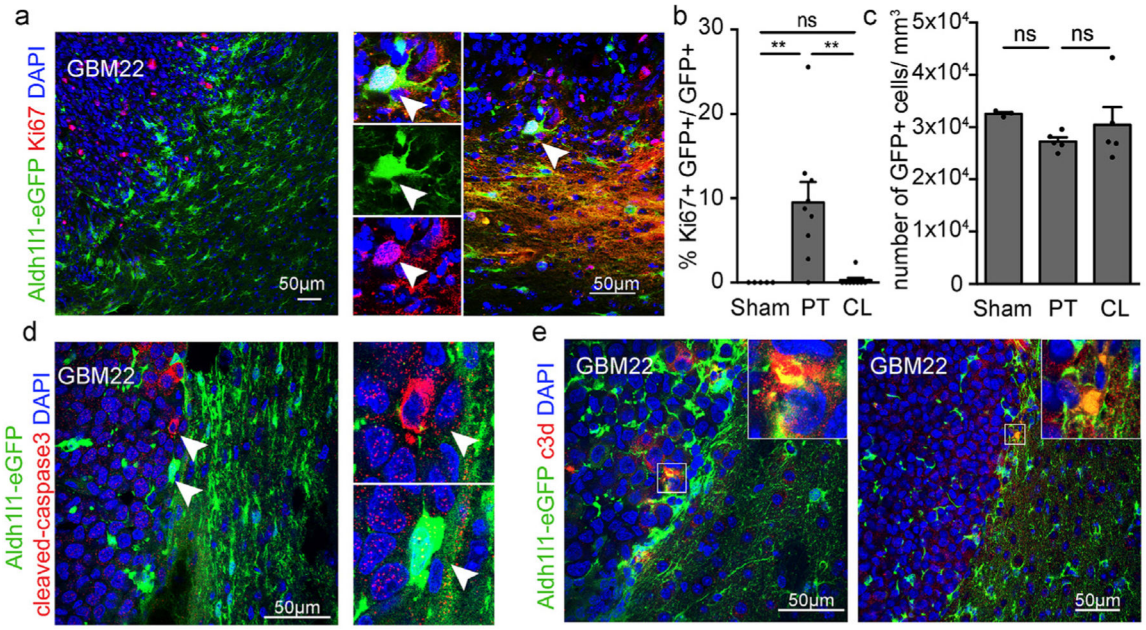

Fig. 4.

Peritumoral astrocytes re-enter the cell cycle, do not undergo apoptosis or express C3d. **a.** Confocal image of Aldh1l1-eGFP + astrocytes co-labeled with the proliferation marker Ki67 in the cortical gray matter surrounding a Jx22 glioma revealed that a subpopulation of peritumoral astrocytes proliferated. White arrowhead points to a Aldh1l1-eGFP Ki67 double-positive astrocyte. **b.** Quantitative analysis of the percentage of Aldh1l1-eGFP Ki67 double-positive astrocytes among all astrocytes. **c.** Quantitative analysis of the number of Aldh1l1-eGFP + cells per mm3 in Sham, peritumoral area and contralateral. Difference in the astrocytic density was not detected (a,b,c n = 10 glioma, 5 sham). **d.** Confocal image of Aldh1l1-eGFP + brain slice labeled with cleaved-caspase-3 antibody, an apoptotic marker, shows a lack of Aldh1l1-eGFP astrocytes co-labeled with cleaved-caspase-3. Some GBM22 glioma cells label positive for cleaved-caspase-3. White arrows point a cleaved-caspase-3+ tumor cell and a Aldh1l1-eGFP + astrocyte without cleaved-caspase-3 labelling. **e.** Confocal images of Aldh1l1-eGFP + brain slices co-labeled with two different C3d antibodies (left and right), a marker for neurotoxic astrocytes demonstrates a lack of C3d labeling in Aldh1l1-eGFP-positive astrocytes. High magnification panels show increased immunoreactivity within the tumor mass and at the border that appears to be unspecific and in between Aldh1l1-eGFP + astrocytes (d,e n = 3).

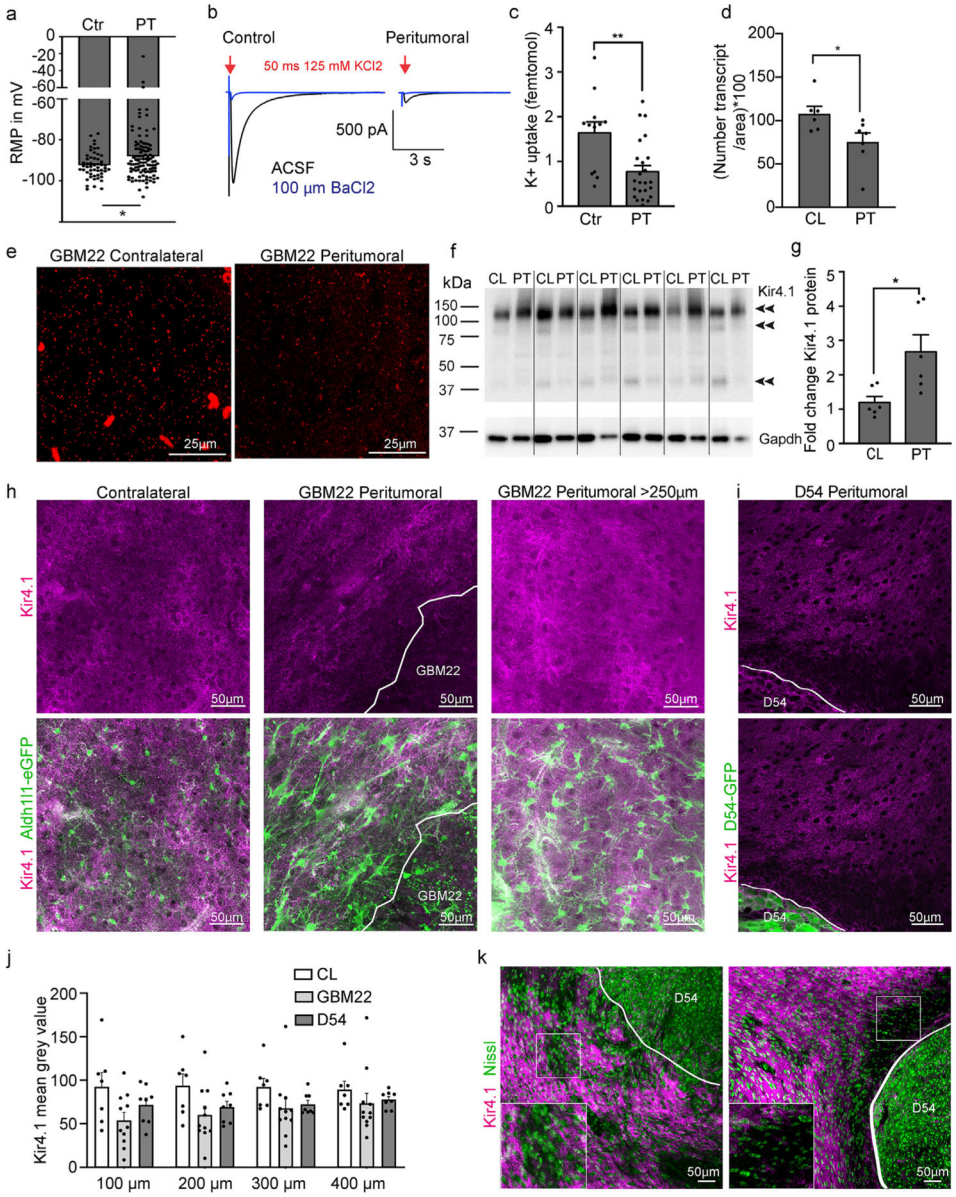

Fig. 5.

Peritumoral astrocytes are impaired in potassium uptake. **a.** Bar graph showing the resting membrane potential (RMP) of peritumoral and control astrocytes. **b.** Potassium current traces elicited by a 50 ms puff of 125 mM KCl before (black) and in the presence of 100 µM Ba^{2+} (blue) in control and peritumoral astrocytes. Cells were voltage-clamped at −80 mV. **c.** Quantification of potassium uptake. **d.** Quantification of KNCJ10 (encodes Kir4.1) transcript numbers. **e.** Representative images of RNAScope (fluorescent in situ hybridization) using probes for KCNJ10. Each small fluorescent dot represents one transcript **f,g.** Western blot and quantification of Kir4.1 protein in peritumoral cortex compared to the contralateral hemisphere (CL). **h.** Immunofluorescence and confocal microscopy of Kir4.1 in the peritumoral and contralateral cortex of Aldh1l1-eGFP GBM22 mice. **i.** Immunofluorescence and confocal microscopy of Kir4.1 in the peritumoral and contralateral cortex of D54 mice.

j. Quantification of Kir4.1 signal intensity. **k.** Double-staining of Kir4.1 and Nissl to assess neuronal density in slices of D54-inoculated mice.

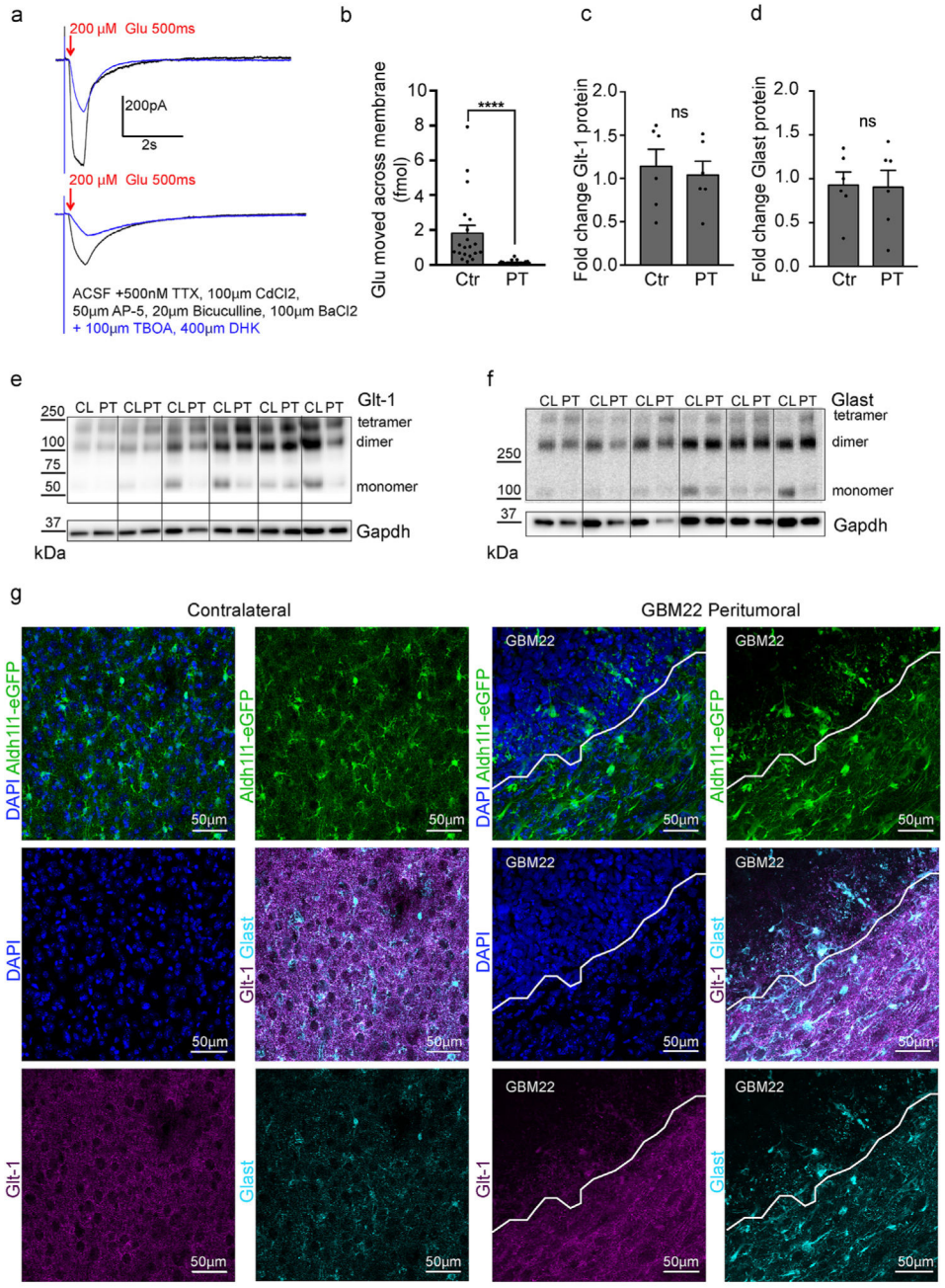

Fig. 6.

Glutamate uptake is impaired in peritumoral astrocytes. **a.** Recordings of glutamate currents evoked by a 200 µM puff of glutamate for 500 ms from control (top) and peritumoral astrocytes before (black) and after the application of the glutamate transporter inhibitors TBOA and DHK (blue). Cells were voltage-clamped at −80 mV. **b.** Quantification of the amount of glutamate that moved across the membrane in control and peritumoral astrocytes. **c-f.** Western blot showing no significant change in Glt-1 (**c,e**) and Glast (**d,f**) protein expression in the peritumoral cortex compared to contralateral cortex. **g.** Confocal imaging

of Glt-1 (magenta) and Glast (cyan) expression in contralateral and peritumoral cortex in Aldh1l1-eGFP mice. High density DAPI-positive nuclei demarcate the tumor border (n = 4).

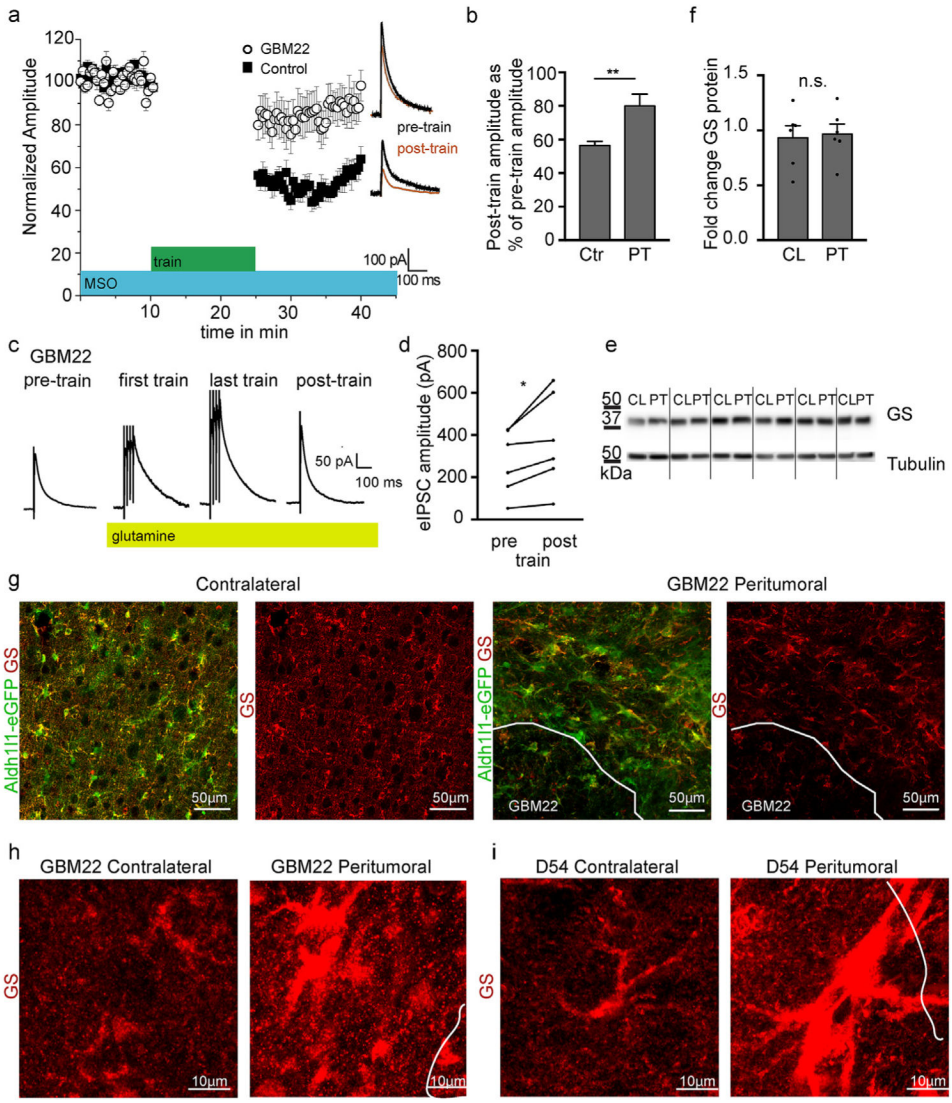

Fig. 7.

Glutamine Synthetase function is impaired in peritumoral astrocytes. **a.** Plot of eIPSC amplitude recorded before and after train stimulation (15 min of 50 Hz and 4 pulse train with 20 s interval) in sham and peritumoral neurons after acute brain slices were incubated in the Glutamine Synthetase (GS) inhibitor methionine sulfoximine (MSO) for at least 90min. **b.** Quantification of post-train eIPSC amplitude normalized to pre-train amplitude. **c.** Representative traces of eIPSCs from peritumoral neurons after adding glutamine before, during and after train stimulation. Traces are averages of 5 consecutive traces before and immediately after train stimulation, and the first and last 5 traces of train stimulation. Application of glutamine increases the amplitude of eIPSCs during and after train stimulation. **d.** Quantification of glutamine-induced change in eIPSC amplitude in response to train stimulation in peritumoral neurons. **e,f.** Western blot analysis and quantification of glutamine synthetase in contralateral and peritumoral cortex. **g.** GBM22 and D54 slices were stained with glutamine synthetase antibody followed by confocal microscopy demonstrating redistribution of the protein into the cell body and main processes

of GBM22 peritumoral astrocytes while GS. **h.** High magnification images of GS in peritumoral astrocytes surrounding GBM22 tumors and in the contralateral hemisphere. **i.** High magnification images of GS in peritumoral astrocytes surrounding D54 tumors and in the contralateral hemisphere. Significantly higher GS levels in D54 peritumoral astrocytes required different image settings compared to the GBM22 samples to demonstrate protein distribution.

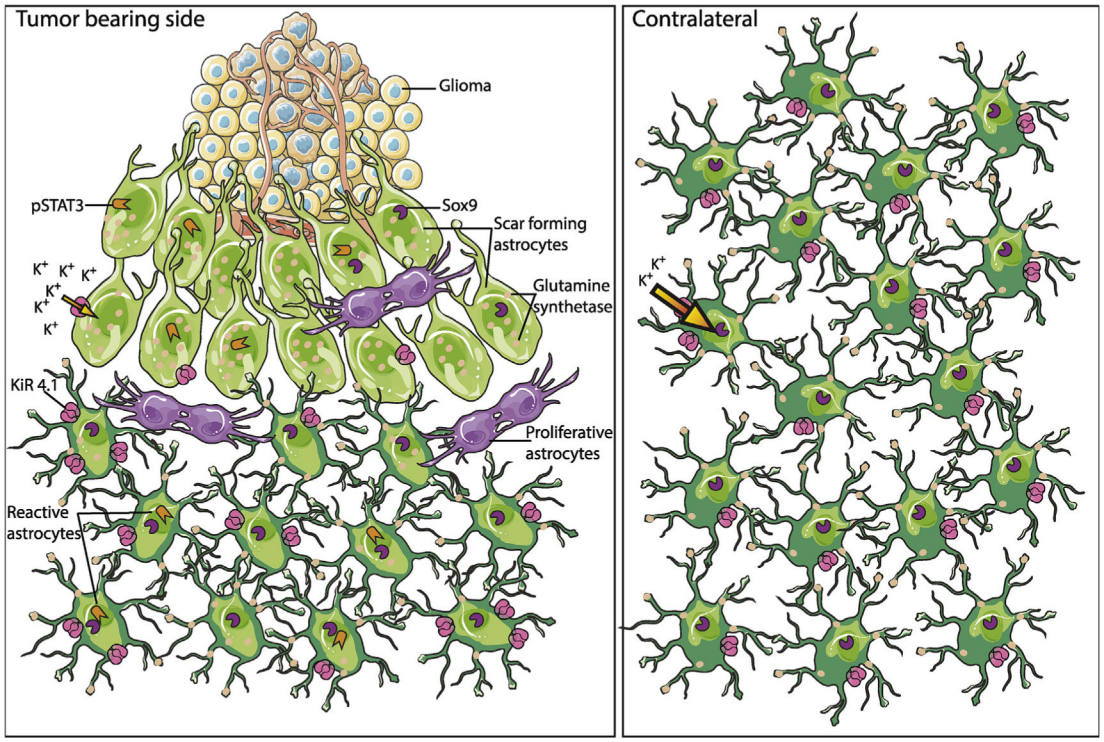

Fig. 8. Working model depicting the dynamic glioma-astrocyte interface.

Peritumoral region in close proximity to the tumor mass consists of mixed populations of proliferating and scar-forming reactive astrocytes characterized by elongated processes and swollen cell soma. Astrocytes at farther distances from the tumor border differ in their molecular profile and lack drastic changes to their morphology. The transcription factor STAT3 is phosphorylated in subset of scar-forming astrocytes that is larger and reaches farther in D54 tumors when compared to GBM22. Astrocytes in the contralateral hemisphere are not pSTAT3-positive. Another transcription factor, Sox9, that labels astrocytes selectively is downregulated in a small subset of scar-forming astrocytes at the tumor border. Glutamine synthetase (GS) expression appeared higher in the cell bodies compared to the processes in scar-forming astrocytes, which is the reverse of the otherwise homogenous expression in contralateral astrocytes. Reactive astrocytes in the peritumoral region exhibit impaired potassium and glutamate uptake due to reduced Kir4.1 protein in some areas and altered localization of glutamate transporter Glt1 respectively, which leads to accumulation of glutamate and potassium in the extracellular environment, thereby contributing to peritumoral hyperexcitability.

Table 1

Reagents used for immunohistochemistry.

Name	Manufacturer	Catalog #	RRID	Species Raised In	Monoclonal/ Polyclonal	Concentration/Pre-treatment
Primary Antibodies						
GFP	Aves Lab	GFP-1020	AB_300798	Chicken	Polyclonal	1:1000
GFAP	Millipore	MAB360	AB_2109815	Mouse	Monoclonal	1:1000
GFAP	Dako	Z0334	AB_10013382	Rabbit	Polyclonal	1:1000
GFAP	Abcam	AB4674	AB_304558	Chicken	Polyclonal	1:1000
Glast	Danbolt	Anti A1, rat GLAST residues 1–25, batch #ab286	(Li et al., 2012)	Sheep	Polyclonal	1.2 mg/ml; 1:6000 (Western Blot)
Glt1	Millipore	AB1783	AB_90949	Guinea Pig	Polyclonal	1:1000 (IHC)
Glt1	Danbolt	anti-B12, rat Glt-1 residues 12–26, batch #ab360	(Holmseth et al., 2005)	Rabbit	Polyclonal	0.2 mg/ml; 1:3500 (Western Blot)
Kir4.1	Alomone	APC035	AB_2040120	Rabbit	Polyclonal	1:400
S100β	Sigma-Aldrich	S2532	AB_477499	Mouse	Monoclonal	1:1000
S100	Dako	0803	Not assigned	Rabbit	Polyclonal	1:1000
Ki-67	Thermo Scientific	RM-9106-S1	AB_149792	Rabbit	Monoclonal	1:100
C3d	R&D systems	AF2655	AB_2066622	Goat	Polyclonal	1:50
C3 (11H9)	Novus Biologicals	NB200-540	AB_10003444	Rat	Monoclonal	1:100 Antigen retrieval in sodium citrate 10 mM pH6.0 30 min at 80 °C
Cleaved-caspase-3	Cell Signaling Technology	9661	AB_2341188	Rabbit	Polyclonal	1:100
Phospho-STAT3 (Tyr705)	Cell Signaling Technology	9145S	AB_2341188	Rabbit	Monoclonal	1:100/Antigen retrieval in EDTA 10 mM-Tris-HCl pH9.0 20 min at 90 °C.
Sox9	Millipore	AB5535	AB_2239761	Rabbit	Polyclonal	1:1000
Secondary Antibodies						
Chicken Alexa-488	Jackson Immuno Research	703-546-155	AB_2340376	Donkey	Polyclonal	1:1000
Chicken Cy3	Jackson Immuno Research	703-166-155	AB_2340364	Donkey	Polyclonal	1:1000
Chicken Alexa-647	Jackson Immuno Research	703-606-155	AB_2340380	Donkey	Polyclonal	1:1000
Rabbit Alexa-488	Jackson Immuno Research	111-546-144	AB_2338057	Goat	Polyclonal	1:1000
Rabbit Cy3	Jackson Immuno Research	111-166-144	AB_2338011	Goat	Polyclonal	1:1000
Rabbit Alexa-647	Jackson Immuno Research	111-606-144	AB_2338083	Goat	Polyclonal	1:1000

Name	Manufacturer	Catalog #	RRID	Species Raised In	Monoclonal/ Polyclonal	Concentration/Pre-treatment
Mouse Alexa-488	Jackson Immuno Research	115-546-003	AB_2338859	Goat	Polyclonal	1:1000
Mouse Cy3	Jackson Immuno Research	115-166-003	AB_2338699	Goat	Polyclonal	1:1000
Mouse Alexa-647	Jackson Immuno Research	115-606-003	AB_2338921	Goat	Polyclonal	1:1000
Rat Alexa-488	Jackson Immuno Research	112-546-003	AB_2338364	Goat	Polyclonal	1:1000
Rat Alexa-488	Jackson Immuno Research	112-546-003	AB_2338253	Goat	Polyclonal	1:1000
Rat Cy3	Jackson Immuno Research	112-166-003	AB_2338253	Goat	Polyclonal	1:1000
Rat Alexa-647	Jackson Immuno Research	112-606-003	AB_2338406	Goat	Polyclonal	1:1000
Guinea pig Alexa-488	Jackson Immuno Research	106-546-003	AB_2337441	Goat	Polyclonal	1:1000
Guinea Pig Cy3	Jackson Immuno Research	106-166-003	AB_2337426	Goat	Polyclonal	1:1000
Guinea Pig Alexa-647	Jackson Immuno Research	106-606-003	AB_2337449	Goat	Polyclonal	1:1000
Goat Alexa-647	Jackson Immuno Research	705-605-003	AB_2340436	Donkey	Polyclonal	1:1000
Dyes						
DAPI	ThermoFisher	D1306	AB_2629482	N/A	N/A	1:1000

Table 2

Reagents used for Western blot analysis.

Name	Manufacturer	Catalog #	RRID	Species Raised In	Monoclonal/Polyclonal	Concentration
Primary Antibodies						
GFAP	Dako	Z0334	AB_10013382	Rabbit	Polyclonal	1:5000
Glt1	Danboldt	B12 ab360	N/A	Rat	Polyclonal	1:3500
Glt1	Millipore	AB1783	AB_90949	Guinea Pig	Polyclonal	1:1000
Glast	Danboldt	A1 #286	N/A	Sheep	Polyclonal	1:6000
Kir4.1	Alomone	APC035	AB_2040120	Rabbit	Polyclonal	1:400
GAPDH	Abcam	AB8245	AB_2107448	Mouse	Monoclonal	1:5000
Tubulin						1:5000
Secondary Antibodies						
Goat anti-rat IgG HRP	Santa Cruz Biotechnology, Inc.	SC2006	AB_1125219	Goat	Polyclonal	1:1500
Goat anti-Sheep IgG HRP	Santa Cruz Biotechnology, Inc.	SC2473	AB_641190	Goat	Polyclonal	1:1500
Goat anti-rabbit IgG HRP	Santa Cruz Biotechnology, Inc.	SC2004	AB_631746	Goat	Polyclonal	1:1500
Goat anti-mouse IgG HRP	Santa Cruz Biotechnology, Inc.	SC2055	AB_631738	Goat	Polyclonal	1:1500
Goat anti-chicken IgG HRP	Santa Cruz Biotechnology, Inc.	SC2901	AB_650515	Goat	Polyclonal	1:1500
Chemiluminescent Substrates						
Clarity Western ECL Substrate- Peroxide Solution		Bio-Rad	102030831	1 min incubation, room temperature		1:2
Clarity Western ECL Substrate- Luminol/Enhancer Solution		Bio-Rad	102030829	1 min incubation, room temperature		1:2